

ANALYSIS OF THE SINTERING FORCE  
IN COPPER

By  
ROGER ALLEN GREGG

A DISSERTATION PRESENTED TO THE GRADUATE COUNCIL OF  
THE UNIVERSITY OF FLORIDA  
IN PARTIAL FULFILLMENT OF THE REQUIREMENTS FOR THE  
DEGREE OF DOCTOR OF PHILOSOPHY

UNIVERSITY OF FLORIDA

1968

Dedicated to

my wife

Susan

## ACKNOWLEDGMENTS

The author wishes to express his sincere gratitude to Dr. F. N. Rhines, chairman of his supervisory committee, for suggesting the subject of this research and for his invaluable assistance in establishing the conceptual framework of the problem.

The author is indebted to Dr. R. T. DeHoff for lending his many talents to the discussion of the problem and especially for his timely contributions to the field of quantitative metallography.

The author wishes to thank Dr. R. E. Reed-Hill, Dr. T. L. Bailey and Dr. R. G. Blake for serving on his supervisory committee.

The financial support of this research by the Atomic Energy Commission was appreciated, and is hereby acknowledged.

## TABLE OF CONTENTS

	Page
ACKNOWLEDGMENTS . . . . .	iii
LIST OF TABLES . . . . .	vii
LIST OF FIGURES . . . . .	viii
ABSTRACT . . . . .	xii
Chapter	
I. INTRODUCTION . . . . .	1
1.1 General Characteristics of the Sintering Process . . . . .	1
1.2 Previous Investigations of the Sintering Process . . . . .	2
1.3 Purpose and Scope of this Research . . . . .	7
II. EXPERIMENTAL PROCEDURE . . . . .	13
2.1 Material Specifications . . . . .	13
2.2 Particle Size Classification . . . . .	14
2.3 Specimen Preparation . . . . .	14
2.4 Experimental Determination of the Sintering Force . . . . .	17
2.41 General features of the apparatus . . . .	17
2.42 Strain measurement . . . . .	21
2.43 Calibration of beam force and deflection versus indicated strain . . . .	21
2.44 Test temperature and environment control . . . . .	23
2.45 Test procedure . . . . .	23

# TABLE OF CONTENTS (Continued)

Chapter	Page
II. (Continued)	
2.5 Post-test Inspection of the Specimens . . . . .	26
2.51 Density determination . . . . .	27
2.52 Metallographic preparation . . . . .	27
2.53 Metallographic examination . . . . .	28
III. EXPERIMENTAL RESULTS . . . . .	30
3.1 Sintering Force . . . . .	30
3.2 Quantitative Metallography . . . . .	38
3.21 Surface area of the void-solid interface	45
3.22 Area tangent count . . . . .	45
3.23 Average mean surface curvature . . . . .	50
3.24 Effect of uniaxial constraint on sintering behavior . . . . .	50
IV. DISCUSSION . . . . .	58
4.1 Surface Energy and Surface Tension of Solids .	59
4.11 Pressure difference across a curved surface . . . . .	61
4.12 Measurement of surface tension effects in solids . . . . .	63
4.2 The Geometry of Sintering . . . . .	69
4.21 The evolution of curvature of the void-solid interface . . . . .	73
4.3 Analysis of the Sintering Force . . . . .	78
4.31 Comparison of predicted and experi- mentally measured sintering forces . . .	83

# TABLE OF CONTENTS (Continued)

Chapter	Page
IV. (Continued)	
4.4 Comparison of the Results of This Research with Previous Investigations . . . . .	89
4.5 Application of the Sintering Force to the Measurement of Surface Tension of Solids . . .	90
4.6 Kinetics of the Sintering Process . . . . .	92
4.61 Estimation of stresses created by external load . . . . .	92
4.62 Correlation of the sintering force with shrinkage rates . . . . .	97
4.63 Comments on the mechanism of shrinkage .	105
V. CONCLUSIONS . . . . .	107
APPENDICES . . . . .	109
I. APPLICATION OF THE PRINCIPLES OF TOPOLOGICAL GEOMETRY TO THE DESCRIPTION OF THE SINTERING PROCESS (after F. N. Rhines [1]) . . . . .	110
II. THE QUANTITATIVE ESTIMATION OF AVERAGE MEAN SURFACE CURVATURE (after R. T. DeHoff [41]) . . . . .	116
REFERENCES . . . . .	122
BIOGRAPHICAL SKETCH . . . . .	126

# LIST OF TABLES

Table	Page
1. Experimental values of sintering force for the 48 micron particle size as a function of density and temperature . . . . .	31
2. Experimental values of sintering force for the 30 micron particle size as a function of density and temperature . . . . .	33
3. Experimental values of sintering force for the 12 micron particle size as a function of density and temperature . . . . .	35
4. Quantitative metallography data for the 48 micron particle size as a function of density and temperature . . . . .	39
5. Quantitative metallography data for the 30 micron particle size as a function of density and temperature . . . . .	41
6. Quantitative metallography data for the 12 micron particle size as a function of density and temperature . . . . .	43

# LIST OF FIGURES

Figure	Page
1. Split graphite mold used for presintering the sintering force specimens . . . . .	15
2. Schematic presentation of experimental setup for determination of the sintering force . . . . .	18
3. Apparatus used for measurement of the sintering force . .	19
4. Cantilever beam assembly of sintering force apparatus . .	20
5. Calibration curves of indicated strain and change in specimen length, $\Delta L$ , versus cantilever beam force . . .	22
6. Typical specimen behavior during experimental measurement of the sintering force . . . . .	25
7. Experimental values of the sintering force as a function of density for the 48 micron particle size spherical copper powder . . . . .	32
8. Experimental values of the sintering force as a function of density for the 30 micron particle size spherical copper powder . . . . .	34
9. Experimental values of the sintering force as a function of density for the 12 micron particle size spherical copper powder . . . . .	36
10. Variation of surface area per unit volume with density for the 48 micron particle size spherical copper powder . . . . .	40
11. Variation of surface area per unit volume with density for the 30 micron particle size spherical copper powder . . . . .	42
12. Variation of surface area per unit volume with density for the 12 micron particle size spherical copper powder . . . . .	44



# LIST OF FIGURES (Continued)

Figure	Page
13. Comparison of the linear relationships between density and surface area per unit volume for the 48, 30 and 12 micron particle sizes . . . . .	46
14. Variation of the net area tangent count with density for the 48 micron particle size spherical copper powder . . . . .	47
15. Variation of the net area tangent count with density for the 30 micron particle size spherical copper powder . . . . .	48
16. Variation of the net area tangent count with density for the 12 micron particle size spherical copper powder . . . . .	49
17. Variation of the average mean curvature of the void-solid interface with density for the 48 micron particle size spherical copper powder . . . .	51
18. Variation of the average mean curvature of the void-solid interface with density for the 30 micron particle size spherical copper powder . . . .	52
19. Variation of the average mean curvature of the void-solid interface with density for the 12 micron particle size spherical copper powder . . . .	53
20. Correlation of the slope of the surface area-density relationship with initial particle size for spherical copper powder . . . . .	55
21. Cross-sectional areas of sintering force specimens after testing . . . . .	56
22. Schematic of surface stresses in a solid . . . . .	60
23. Resolution of surface tension into a pressure acting normal to each point of a curved surface . . . . .	62
24. Two arrangements for balancing the shrinkage of metal foils by inducing creep with an external force .	65
25. Schematic of surface tension forces and grain boundary array in wire geometry used for determination of surface tension in metals . . . . .	68

# LIST OF FIGURES (Continued)

Figure	Page
26. Variation of genus (connectivity) and number of separate parts of the void-solid interface with density for the 48 micron special copper powder [43] .	72
27. Comparison of the average surface curvature as a function of density for the 48, 30 and 12 micron particle sizes of spherical copper powders . . . . .	74
28. Variation of average surface curvature with density for a mixture of sizes of an irregular, dendritic, electrolytic copper powder [62] . . . . .	79
29. Resolution of surface tension forces emanating from the cut surface of a spherical pore in a direction perpendicular to the sectioning plane . . . . .	81
30. Comparison of the experimental values of the sintering force with predicted values for the 48 micron particle size powder . . . . .	84
31. Comparison of the experimental values of the sintering force with predicted values for the 30 micron particle size powder . . . . .	35
32. Comparison of the experimental values of the sintering force with predicted values for the 12 micron particle size powder . . . . .	86
33. Room temperature yield stress at 2 per cent elongation as a function of density for a range of particle sizes of the spherical copper powders used in this investigation [67] . . . . .	94
34. Variation of the average solid area and the effective solid area estimated from experimentally observed mechanical behavior with density for spherical copper powders . . . . .	96
35. Estimated operating stresses created by externally applied force on sintering force specimens . . . . .	98
36. The relation between strain rate, $\dot{\epsilon}$ , and stress, $\sigma$ , as affected by the scale of the microstructure for isothermal high temperature deformation of pure metals . . . . .	100

# LIST OF FIGURES (Continued)

Figure	Page
37. Variation of experimentally determined linear shrinkage rates with density for the 48 [70] and 30 [71] micron particle sizes of spherical copper powder . . . . .	101
38. Relationship between linear shrinkage rates and estimated effective stresses for the 48 and 30 micron particle sizes of spherical copper powder . . . . .	102
39. Correlation of linear shrinkage rate--estimated operating stress relationship with deformation rate law based on stress-directed diffusion . . . . .	104
40(a). Examples of bodies bounded by surface of genus zero, one and two . . . . .	112
40(b). Variation of genus with number of contacts per particle . . . . .	112
41(a). Separation of sintering into three stages on the basis of changes in genus of the void-solid interface . . . . .	114
41(b). Effect of genus of the void-solid interface on its minimal surface area configuration . . . . .	114
42. Orientation relationships that exist between an arbitrary element of surface ( $dudv$ ) and a sectioning plane; $\hat{n}$ is the surface normal; $\hat{u}$ and $\hat{v}$ are the directions of principal curvature; $\hat{k}$ is normal to the sectioning plane . . . . .	120

Abstract of Dissertation Presented to the Graduate Council  
in Partial Fulfillment of the Requirements for the  
Degree of Doctor of Philosophy

ANALYSIS OF THE SINTERING FORCE IN COPPER

By

Roger Allen Gregg

June, 1968

Chairman: Dr. F. N. Rhines

Major Department: Metallurgical and  
Materials Engineering

The sintering force is defined as the external load which will balance the contractile tendency of a sinter body in the direction of its application. Experimental measurements of the sintering force were made upon uncompacted, sintered copper specimens as a function of apparent density, sintering temperature and particle size. All measurements were obtained from specimens sintering in dry, deoxidized hydrogen.

Measurements of void volume and of surface area and average mean curvature of the void-solid interface were made through the procedures of quantitative metallography.

The sintering force was found to increase from zero at the onset of sintering, pass through a maximum at approximately 90 per cent of theoretical density and decrease toward zero at bulk density. This general behavior was observed for each particle size. The magnitude of the sintering force at any density increased with a decrease in particle size. There was no effect of temperature on the sintering force in copper over the range 950 to 1050°C.

The surface area per unit volume-density relationship was observed to be linear for each particle size. Variation of the average mean surface curvature with density was found to be qualitatively identical to that observed for the sintering force.

The results are analyzed on the basis of a balance between the externally applied force and the surface tension forces promoting shrinkage. A quantitative expression of the sintering force in terms of the surface geometry and surface tension of the sinter body is derived from basic concepts of capillarity. A comparison is made of the sintering forces predicted by this relation and experimental values.

Sensitivity of the rate of shrinkage to the geometry of the microstructure of the sinter body will be demonstrated through simultaneous application of the concept of the sintering force, an empirical treatment of the mechanical behavior of the sinter body and a stress-strain rate relation based on deformation by creep.

## CHAPTER I

### INTRODUCTION

The atoms or molecules on the free surface of a solid possess higher energy than those within the interior. Therefore, a solid system comprised of finely divided powders has higher total energy than a single large particle of the same material and equal mass. By rearranging material so as to reduce its surface area, the system of powder particles can lower its energy and become thermodynamically more stable. When powder particles are held in contact at a temperature close to, but below, their melting point, material rearrangement driven by the excess surface energy can produce permanent adherence between the particles and result in a single, solid framework. This process is known as sintering. Most powdered materials will exhibit sintering under the proper conditions of temperature and environment. This includes crystalline, vitreous and organic materials.

#### 1.1 General Characteristics of the Sintering Process

When powdered materials are sintered the following general features are observed. The particles form permanent connections at their points of contact, which increase in size with time. The surfaces of the pores become smooth and the total volume of porosity within the powder aggregate decreases with time, increasing the apparent density of the system. Every geometric change driven by surface

energy is accompanied by a decrease in the total surface area in the system. Under the proper conditions, the apparent density of the sinter body may approach the absolute density of the solid material.

The evolution of the internal structure of a sinter body is separable into stages. The classification of the stages of sintering as proposed by Rhines [1]\* will be applied here. In the first stage, particle contacts broaden into weld necks and surface contours are smoothed. In the second stage, the principal geometric change is a decrease in connectivity of the pore network through closure of the connecting links, or channels, of the network. The completion of this process signifies the end of the second stage. The third and final stage is characterized by the elimination of the isolated porosity.

## 1.2 Previous Investigations of the Sintering Process

Considerable effort has been expended in fundamental research of sintering, primarily directed toward determination of the controlling mechanism. There exist several mass transport processes which can act either individually or in concert in their participation in the material rearrangement observed during sintering. These are: evaporation-condensation, surface diffusion, volume diffusion, viscous flow and bulk deformation by shear processes. Consequently, sintering is a complex phenomenon, a fact evident in the diversity of the theories of sintering which have been proposed.

Saurwald, in a series of papers, was the first to attempt to formulate a general theory of sintering. He concluded [2] that adhesive

---

\* Numbers in brackets refer to the references.

forces between the powder particles are responsible for their consolidation, which in his opinion, had striking similarities to the recrystallization processes observed in metals. Balshin [3,4,5] attempted a refinement of this approach suggesting that densification would result from recrystallization initiated at particle contacts, while a decrease in density would be produced by recrystallization within the particles. Jones [6] agreed that the forces of atomic cohesion determine the sintering process and concluded that since these forces decrease with increasing temperature, the increase in sintering rate with temperature is due to a rapid decrease in the resistance to plastic flow. Balke [7], Wretblad and Wulff [8], and also Rhines [9], were among the first to suggest that surface tension played a major role in promoting sintering. Balke visualized a "zipper action" in closure of the void space which was initiated at the contact points between the particles. Wretblad and Wulff suggested the application of the equations of capillarity in calculating the stresses at the contact points as a function of the shape of the solid surfaces and their energy. They further suggested that the stresses estimated in this manner could exceed the elastic strength of the solid and result in plastic deformation. Rhines concurred that the magnitude of the forces derived from surface tension would be greatest in the regions of highly curved surfaces. Interest in this viewpoint was spurred by theoretical [10,11] and experimental analyses [12] of the viscous flow of metals under the action of surface tension. It is now generally agreed that surface tension is the primary force in achieving the geometric changes observed during sintering. However, agreement has not been reached



concerning the manner in which the action of surface tension accomplishes these changes.

Pines [13] and also Shaler and Wulff [14] suggested that the mechanism(s) responsible for smoothing the particle surfaces and rounding the pores could be distinct from the transport mode producing densification. Shaler and Wulff pointed out that densification requires changes in shape and size of the particle network or "skeleton." In order to achieve this, material must be removed from within the particles along the line joining their centers. It is now generally acknowledged [15,16,17] that transport mechanisms which are restricted to the surface, such as evaporation-condensation and surface diffusion, can produce only surface-rounding, not densification. Rhines [18] made the important suggestion that a transfer of void "space" from the pores to the external surface, which would produce densification, could occur by a lattice vacancy diffusion process.

To avoid the complications of a multiconnected, three-dimensional stack of particles, Kuczynski [19] used simple models of a single sphere on a flat surface and two spheres in contact to evaluate the controlling mechanism in the first stage of sintering. He invoked the equations of capillarity to calculate the vapor pressure, vacancy concentration and internal pressure in terms of surface geometry. For these simple geometries he was able to derive equations relating the rate of growth of the weld neck to the transport mechanism assumed. His experimental evidence on metals [19] indicated that neck growth was controlled by volume diffusion in coarse particle systems, and by surface diffusion for small particles. In glass [20] he reported

a viscous flow mechanism. Mackenzie and Shuttleworth [21] pointed out that the removal of vacancies by volume diffusion to the exterior of the sinter body is too slow to explain the rates of densification observed. In addition, densification by this process would progress inward from the external surface,\* and the rate of densification would be a function of the size and shape of the system; a situation which does not develop in sintering.

Using the technique of wrapping wires on a spool, Geach and Jones [23] observed that the grain boundaries formed at contact points were stable for long periods of time at sintering temperatures. Using the same experimental procedure, Alexander and Balluffi [24] claimed that pores in the wire compact continued to shrink only if they remained connected to a grain boundary. Correa da Silva and Mehl [25] and Pranatis et al. [26] suggested that vacancy removal, required for densification by volume diffusion, could occur at grain boundaries through collapse of the vacancies collected there; Herring [11] had previously suggested this mechanism for creep by volume diffusion. Kuczynski [27] adopted the grain boundary effect into his diffusion model and found reasonable agreement between the rates of pore closure predicted by volume diffusion and those observed in photographs of wire-compacts published by Alexander and Balluffi [24,28].

Herring [29] showed that in two-particle systems with similar geometries but differing by a scale factor  $\lambda$ , the times required to reach identical stages in sintering should be related through this

---

\* This has been reported by Rhines et al. [22] to occur only in the pores immediately adjacent to the external surface.

factor. If, for example,  $(\text{powder})_1$  is  $\lambda$  times larger than  $(\text{powder})_2$ , then the times required to reach similar stages of sintering are given by

$$\frac{\Delta t_1}{\Delta t_2} = \lambda^n$$

where

- $n = 1$ , for evaporation-condensation;
- $n = 2$ , for viscous flow;
- $n = 3$ , for volume diffusion; and
- $n = 4$ , for surface diffusion.

Alexander and Balluffi tested this relation for their wire compacts and found reasonable support for volume diffusion.

However, DeHoff et al. [30] applied Herring's analysis to the rate of weld neck growth between twisted wires and found the exponent,  $n$ , to vary with the size of the wires. Small wires moved together during sintering while large wires did not, thereby resulting in dissimilar geometries and making Herring's analysis inapplicable.

Shewmon and Wilson [31] measured the shrinkage and weld neck size during sintering of chains of particles. They reported that less than 10 per cent of the volume of the weld neck resulted from shrinkage, an observation which casts doubt on the ability of Kuczynski's model to reveal the mechanism of densification. They reported that Herring's analysis supported surface diffusion as the mechanism for weld neck growth.

Mackenzie and Shuttleworth [21] chose to support the point of view that surface tension, acting through the curvature of the pore surface, creates stresses sufficient to result in macroscopic plastic

deformation of the solid framework. They derived a relation for rate of densification based on the interaction of the capillary pressure of the pores in raising the stress level in the solid between the pores past that required for yielding. Clark and White [32] and Clark, Cannon and White [33] developed a model based on viscous flow, within a surface layer, under the forces of surface tension. They applied their model, and also the equation of Mackenzie and Shuttleworth, to experimental densification rates and achieved some degree of fit.

Rhines and Cannon [34] found that the application of small compressive loads to a sintering system had the same effect on densification rates as an increase in stress level has on creep rates. In other words, no new mechanism was introduced through the application of small compressive loads to the sinter body. Williams and Westmacott [35] showed that one of the accepted rate equations for transient creep of metals could be used to develop a relation for rate of weld neck growth which is so similar to Kuczynski's equation supporting volume diffusion, that the available experimental data could not distinguish between them. Lenel and co-workers [17,36] have observed that the effect on shrinkage rate produced by varying the level of small compressive stresses is predictable from creep equations based on deformation by dislocation processes.

### 1.3 Purpose and Scope of this Research

In spite of the obvious differences in the conclusions drawn in the theoretical and experimental analyses of sintering, there exist some important consistencies:

- (a) surface tension is the force through which densification is achieved, and
- (b) the magnitude of the effect of surface tension is determined by the geometry of the void-solid interface.

Recognition of the importance of statement (b) provoked the use of the simple spherical models of Kuczynski, the wire compacts of Alexander and Balluffi and the particle chains of Wilson and Shewmon. The complex theories of Mackenzie and Shuttleworth, and of Clark and co-workers are also based on geometric effects consistent with statements (a) and (b). However, direct experimental evidence that surface tension is the force which produces densification has never been satisfactorily obtained, nor has the relationship between surface tension and the geometry of the void-solid interface in real sintering systems been defined.

The first detailed study of the geometrical evolution of the pore structure during sintering was published by Rhines et al. [22]. They reported that although the total volume and number of pores decreased with increasing density, the average pore size increased. Arthur [37] measured the relative amounts of interconnected and closed porosity and found the porosity to be mainly interconnected; only after reaching a density of approximately 95 per cent of theoretical density does the porosity become completely closed to the external surface. Both of these results were unexpected and clearly revealed the inadequacies of simple models in explaining the behavior of real complex systems.

Rhines [1] has shown that application of the principles of descriptive topology to sintered structures provides a simplified

method for describing the complex geometric changes observed. In developing this approach (see Appendix I), Rhines pointed out that the minimal surface area possible is a function of the degree of connectivity of the void-solid surface; i.e., the topological state. As the connectivity decreases, the minimal area decreases; thus, once minimal configuration has been reached, further decrease in surface area requires a decrease in connectivity of the surface. DeHoff et al. [38] have produced experimental evidence that, in the second stage of sintering, a linear correspondence exists between the density of the sintered system and the surface area it contains in unit volume. This behavior has been found to hold for all shapes, sizes, and compositions of powdered materials investigated, demonstrating the existence of a unique geometrical evolution for all sintering systems. In addition, they also reported that the slope of the linear relationship was predetermined by the initial connectivity of the particle stack. Recently, Barrett and Yust [39] have demonstrated by serial sectioning technique that the isolated parts of the porosity network which are developed in the second stage of sintering "occur first as widespread volumes of interconnected porosity, definitely nonspherical in shape." They concluded that these sections of the void volume become separated from the rest of the porous network, and from the external surface of the sinter body, by the closing of parts of the void; a similar process has previously been described by DeHoff et al. [38] as a closure of channels in the porous network.

Techniques for quantitative determination of many of the geometric variables which characterize sintering (e.g., volume fraction

of porosity, surface area and mean free path in the void or solid phases) have been available for some time [40]. Recently, DeHoff [41] and Cahn [42], in simultaneous and independent efforts, developed a new fundamental relationship of quantitative metallography which permits the experimental determination of the average value of the mean surface curvature over the total void-solid interface. The details of the derivation of this important relation are presented in Appendix II.

A technique for experimental determination of the topological properties of sintered structures has been presented by Aigeltinger [43]. In his procedure a series of closely spaced microsections, obtained by the use of a microtome, is used to synthesize the structure. Thus, the degree of connectivity of the void-solid surface and the number of isolated parts of the porosity can be determined as a function of the density of the sinter body.

The geometric and topological information now available certainly constitutes a significant basis for understanding the sintering behavior of real systems. However, in order to explain the kinetics of sintering it is necessary to discover the relations which exist between the kinetics and the geometry of the sintered structure. Rhines [44] has suggested that insight into the latter problem might be gained by an analysis of the force of contraction generated by a sintering powder system. Since the mechanical equivalent to the sintering force exists regardless of the mechanism through which the solid responds to the thermodynamic driving forces, no a priori assumptions as to operative mechanism need be made in order to use this approach.

Except for the minor effects of gravity [45], sinter bodies shrink isotropically. In order to stop total shrinkage, and in effect balance the force of sintering isotropically, a uniform hydrostatic tension would have to be imposed on the sinter body. Since it is not practical to achieve this condition experimentally, the sintering force has been defined by Rhines [44] as the force necessary to stop the contraction of the sinter body in the direction of an uniaxially applied load.

An attempt to measure such forces was made by Young [46]. He used the method which was employed by Udin [12] to measure surface tension effects in fine metal wires. By suspending various weights from a series of identically prepared, sintered specimens, Young was able to determine the load which just balanced the tendency to contract in the direction of the applied load. He reported that, in irregularly shaped -325 mesh copper powder, the sintering force increased with increasing density over the range of densities he investigated; from 45 to 60 per cent of the theoretical density. However, he was unable to discern any apparent relation between this unexpected\* functional dependence on density of these external forces, and the internal forces which are expected to be determined by the geometric evolution accompanying densification.

It was the purpose of this research to develop more completely the concept of the sintering force, experimentally measure it and

---

\* Intuitively, the force of sintering would be expected to decrease with increasing density since sintering rates decrease sharply (often several orders of magnitude) with increasing density.



determine phenomenologically its relation to the physical, geometric and mechanical properties of the sintered structure. If these goals can be achieved, a strong link between geometry and kinetics will have been forged.

The sintering behavior of a system of powder particles is largely determined by the characteristics of the powder. Therefore, the choice of the material used in this exploratory research effort was predicated by the necessity for easily controlled experimental variables and a high degree of reproducibility in the qualities of the sintered specimens. For these reasons, copper was chosen and has the following desirable features:

- (1) reliable experimental values of surface tension,
- (2) unique compatibility with hydrogen as the sintering environment;
  - (a) all oxides of copper are reduced by hydrogen,
  - (b) the high diffusivity of hydrogen in copper prevents any pressure buildup within closed porosity,
- (3) a melting point ( $1083^{\circ}\text{C}$ ) which creates no serious experimental difficulties, and
- (4) mechanical properties as a function of stress and temperature which are documented as completely as for any metal.

## CHAPTER II

### EXPERIMENTAL PROCEDURE

#### 2.1 Material Specifications

The work of DeHoff et al. [38] made quite clear the importance of the topological state of the initial particle stack in determining the specific path of geometrical evolution observed during densification. They pointed out that the most efficient stacking for any given particle shape is never achieved, and it is generally possible to increase the number of contacts per particle by vibratory packing or mechanical compaction. The latter was not a part of the experimental procedure in this research. However, it was necessary to handle the mold after filling it with powder; therefore a powder which would produce a stable and reproducible stack was highly desirable. In this respect particle shape is of primary importance, for it has been known [47,48] for some time that, in general, spherical powders produce the most efficient, and consequently the most stable, loose particle stacking. The copper powders employed in this investigation were prepared by the Linde Company by atomization of liquid copper in an inert gas atmosphere. The powders possessed a high degree of sphericity and were of high purity. Of particular importance to the geometric analysis of the sintered structure, the amount of copper oxide within the interior of the particles was negligible and the formation of gas

porosity, which results from the reduction of internal copper oxide by the hydrogen sintering atmosphere, was also negligible.

## 2.2 Particle Size Classification

Standard ASTM sieve analysis procedures were used for particle size classification. In this method, the number which is used to designate a sieve size corresponds either to the average number of apertures per square inch in the wire mesh screen or to the average size of the apertures. If the particles will pass through a sieve, a minus (-) sign precedes the sieve size number; a plus (+) sign precedes the number for a sieve through which the particles will not pass.

The powder used in this investigation was initially separated into two size classes: -270 + 325 mesh (-52 + 44 microns) and -325 mesh (-44 microns) on a standard Ro-Tap mechanical shaker. Later in the course of the work the -325 mesh powder was used as the source of a -20 micron classification performed on an Allen-Bradley Sonic Sifter. The particle size distribution, as reported by the powder manufacturer, was used to calculate the average particle diameters within each size classification. The average diameters for the -52 + 44, -44 and -20 micron sizes were estimated to be 48, 30 and 12 microns, respectively.

## 2.3 Specimen Preparation

Specimens used for measurement of the sintering force were prepared by presintering to the desired shape in the split graphite mold shown in Figure 1. The basic shape of the specimen was similar to a cylindrical tensile test specimen. However, the shoulders at each end of the reduced section were gently sloped to reduce constraint at these

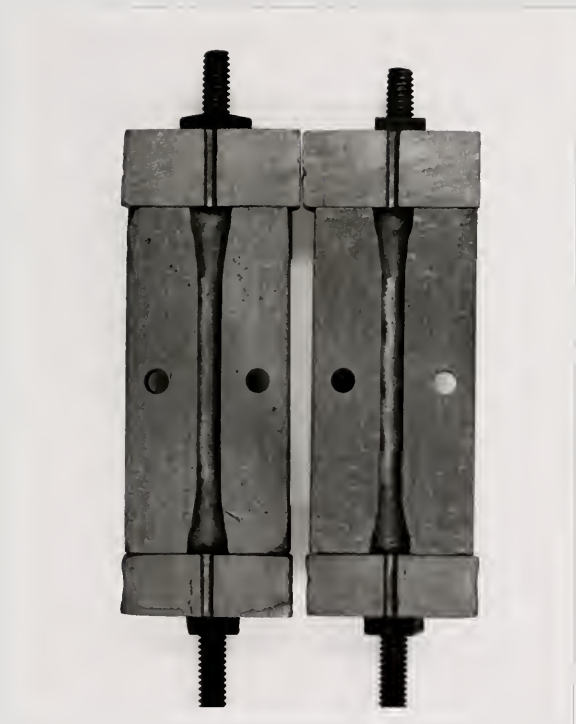


Figure 1. Split graphite mold used for presintering the sintering force specimens.

positions while the specimen was shrinking during presintering or cooling from the presintering temperature. Connection between the specimen and the load column was provided by presintering 0.9375 inch diameter tungsten rods into each end of the specimen. The tips of the rods embedded in the specimen were notched to provide interlocking between the tungsten and the copper and increase the mechanical strength of the connection.

All specimens were presintered at  $700^{\circ}\text{C}$  in dry, deoxidized hydrogen. Presintering times were 15, 20 and 30 minutes for the 48, 30 and 12 micron particle sizes, respectively. The density of the loose particle stack prior to presintering was calculated by determining the volume of the mold (by filling with water) and weighing the volume of the powder which filled the mold. Several determinations of the loose-stack density revealed it to be very reproducible and always between 5.1 and 5.3 gms per  $\text{cm}^3$  for each particle size. The densities of the presintered specimens were found to lie in the range 5.4 to 5.6 gms per  $\text{cm}^3$ .

As a result of storage and handling in humid atmospheres the powder particles were covered with thin oxide films. No attempt was made to remove these films before presintering; however, close inspection after presintering revealed all surfaces, both internal and external to the specimen, were clean and bright. Internal surfaces were inspected in specimens fractured immediately after presintering.

## 2.4 Experimental Determination of the Sintering Force

### 2.4.1 General features of the apparatus

The apparatus used for measurement of the sintering force, shown schematically in Figure 2, was designed to provide the following:

- (1) A continuously variable and manually adjustable force which would permit the application of the instantaneous force required to stop contraction of the sintering specimen at any given density.
- (2) Maximum sensitivity to change in specimen length; required to measure accurately the sintering force at high densities where shrinkage rates are extremely slow.
- (3) Easy entry and removal of the specimen from the test rig; required due to the weakness of the presintered specimens and in order to preserve the density which existed at the moment of final force measurement.
- (4) Minimum deleterious effects from changes in ambient and furnace temperature so that the control possible for these variables would be adequate.

Simultaneous application and measurement of the externally applied load as well as direct measurement of length changes in the specimen were accomplished through the use of the cantilever beam assembly in Figure 3. Length changes were revealed by the change in beam deflection: beam force was monitored by measurement of the strain created in the beam by its deflection.

The design of the beam is shown in Figure 4. The reduced section of the beam provided a location of concentrated stress in the region of the fillet where measurable strain was maximized for a given deflection. The beam was fabricated from an iron-base material, Iso-elastic alloy, so named for its low temperature coefficient of the elastic modulus. As reported by the alloy supplier, J. Chatillon and Sons, the value of

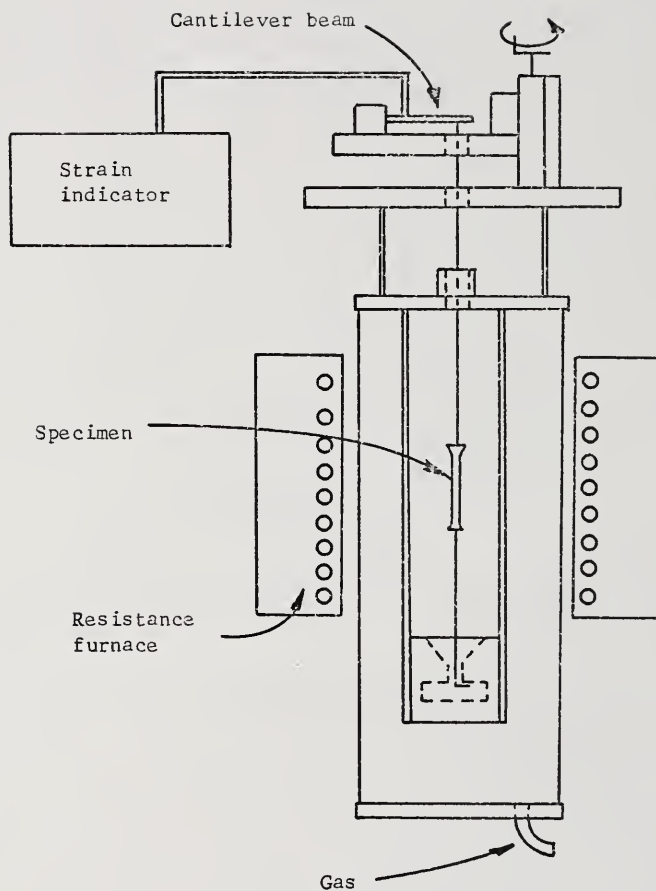


Figure 2. Schematic presentation of experimental setup for determination of the sintering force.



Figure 3. Apparatus used for measurement of the sintering force.



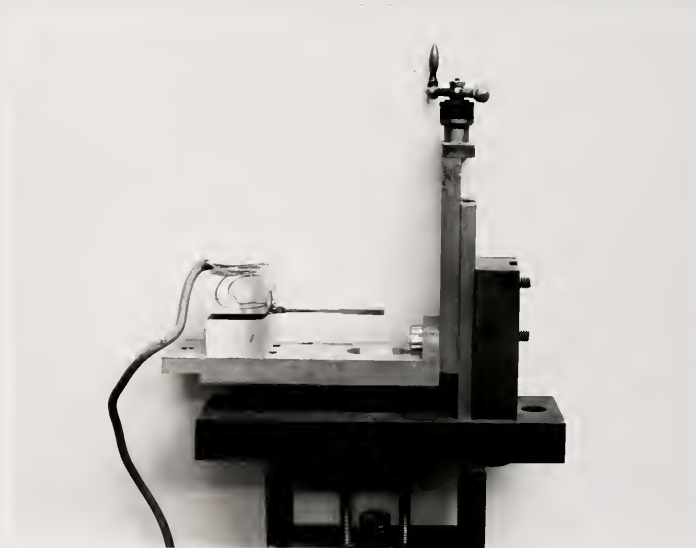


Figure 4. Cantilever beam assembly of sintering force apparatus.

this coefficient for this alloy was  $\pm 20 \times 10^{-6}$  per  $^{\circ}\text{F}$  as compared to a value of  $-190 \times 10^{-6}$  per  $^{\circ}\text{F}$  for spring steel. In addition, errors due to anelastic and hysteresis effects in this material were also small; .02 and .05 per cent of the total deflection, respectively.

#### 2.42 Strain measurement

The output of the four strain gages employed on the beam was measured by a Baldwin-Lima-Hamilton model 120 A strain indicator. Two gages each were placed on the top and bottom sides of the beam near the fillet farthest from the free end of the beam. The arrangement of the gages into the Wheatstone Bridge of the strain indicator served two purposes:

- (1) Measurable strain was increased by a factor of four over the true strain at this position of the beam.
- (2) Strains induced in the gages by thermal expansion or contraction of the beam were essentially cancelled.

#### 2.43 Calibration of beam force and deflection versus indicated strain

In order to know accurately the beam force as a function of total indicated strain, standard weights were applied to the beam and the resultant strain recorded. The deflection of the beam, as a function of beam force, was determined by direct measurement with an optical system accurate to  $0.5 \times 10^{-4}$  inches. The calibration curves for these quantities are presented in Figure 5. They were found to be reproducible to within  $\pm 1$  per cent of the value of the beam force. It was assumed that all changes in beam deflection could be attributed to changes in specimen length. Based on the sensitivity of the strain

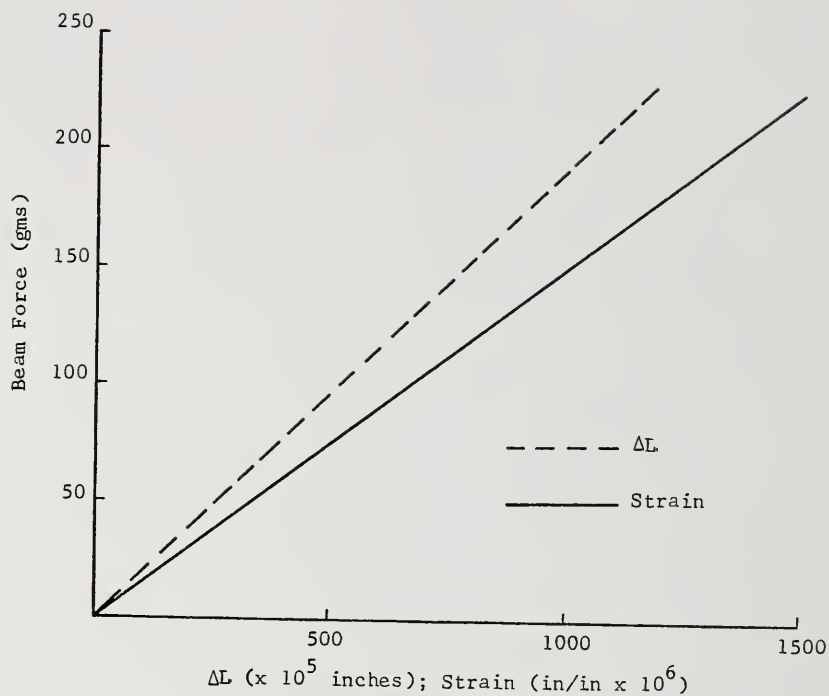


Figure 5. Calibration curves of indicated strain and change in specimen length,  $\Delta L$ , versus cantilever beam force.

indicator to a change in measurable strain of  $2 \times 10^{-6}$ , the apparatus was sensitive to a change of  $3.5 \times 10^{-6}$  inches in specimen length which corresponded to a change of 0.3 gms in beam force.

#### 2.44 Test temperature and environment control

All sintering force tests were made in an atmosphere of dry, deoxidized hydrogen. The gas pressure within the furnace tube was maintained just above atmospheric pressure by constant gas flow to prevent the entry of oxygen into the system. Test temperatures were provided by a nichrome element resistance furnace which had a temperature variation of  $\pm 2.5^{\circ}\text{C}$  over 4 inches of the hot zone. Test temperatures were measured with platinum, platinum-10 per cent rhodium thermocouples and controlled by a Leeds and Northrup Precision Set-Point Control System, which maintained the temperature of the hot zone to within  $\pm 0.1^{\circ}\text{C}$ .

#### 2.45 Test procedure

The presintered specimens were integrated into the load column by inserting the L-shaped end of the upper connecting rod into the end of the pull-rod. With the furnace at the desired test temperature, the load column was lowered into the hydrogen-filled furnace tube. The bottom connecting rod was inserted into a slot at the bottom of the apparatus, lowered below the restraining ledge and then rotated such that elevation of the L-shaped tip of the bottom connecting rod, either by manual adjustment of the beam position or by shrinkage of the specimen, would place the specimen under tensile constraint.

In practice, it was found that the connecting rods were often presintered into the specimen at slight angles to the specimen axis, a situation which produced bending stresses upon initial loading. Therefore, each specimen was either initially brought into creep by manual adjustment of the beam force, or was allowed to shrink against the constraint of the beam for some time. This procedure helped to straighten the load column and produced approximately uniaxial loading during the remainder of the test.

Typical behavior of a specimen during the test is shown in Figure 6. Notice that the use of a cantilever beam to supply the external force results in an inverse relationship between specimen length and the magnitude of the beam force on the specimen. If the specimen can shrink against the initial load, its decrease in length will increase the force which the beam exerts upon it. If, by manual adjustment of the beam position, the force is increased, then the specimen may be made to creep. The elongation of the specimen in creep reduces the beam force on the specimen until the sintering force within the specimen is sufficient to balance the external beam force. This balance of forces is only temporary since radial shrinkage of the specimen is unopposed, and the density of the specimen is constantly increasing. In practice, the time interval over which the forces appeared to be balanced ranged from a few seconds to several hours depending on the shrinkage rate of the specimen, as affected by temperature, particle size and density. The behavior indicated in Figure 6 is that of a specimen whose density would lie in the range where the sintering force was observed to increase with increasing density. Consequently, after

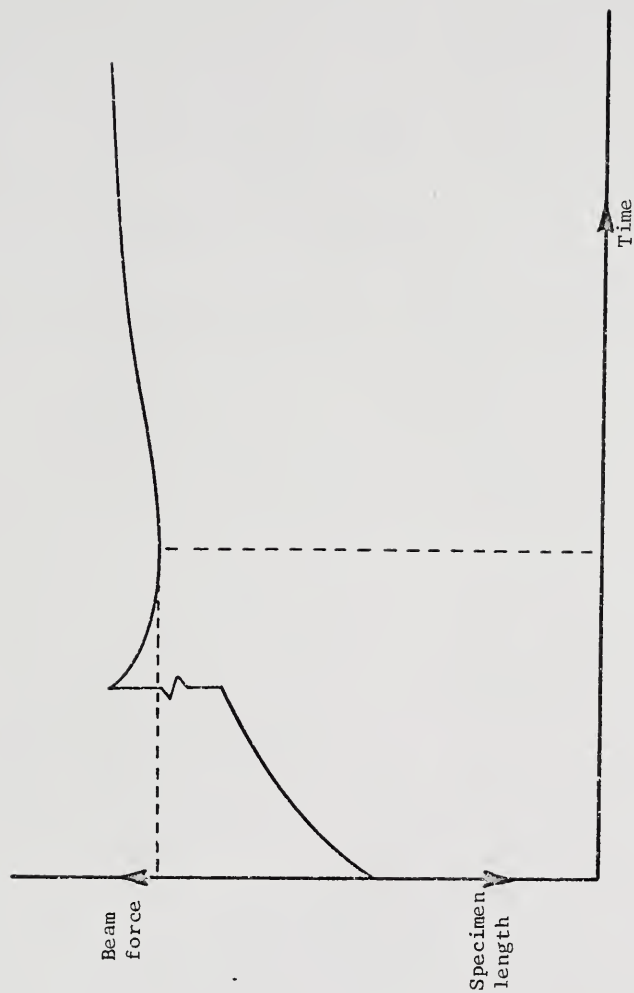


Figure 6. Typical specimen behavior during experimental measurement of the sintering force. The dashed line indicates the desired balance of internal and external forces.

the initial force balance, the external force against which the specimen can shrink increases as the specimen density increases. For specimens in this range of density, the test was aborted at the moment the specimen first revealed that it had progressed from creep to shrinkage. At this point (indicated by dashed lines in Figure 6) the external force was removed by manually lowering the beam support. The specimen was then immediately raised to the cool end of the furnace tube in order to preserve the density which corresponded to the final force measurement.

The bottom of the load column was essentially suspended from the rest of the column, therefore the minimum load on the specimen throughout the test was the beam force plus the weight of the bottom connecting rod. However, since each point along the length of the specimen had to support the weight below it, the average load on the specimen was taken as the sum of the beam force, the weight of the bottom connecting rod and 0.5 times the weight of the specimen.

## 2.5 Post-test Inspection of the Specimens

After testing, each specimen was inspected for excessive bending, necking or obvious failures due to cracks. Any specimen which possessed any of these defects after testing was discarded. As a further check on uniformity the diameter of the cylindrical specimen was measured at several locations along the gage length. A Jones and Lamson optical comparator with a reported accuracy of 0.0001 inch was used for this purpose.

## 2.51 Density determination

Apparent densities of tested specimens were determined through Archimedes principle using the standard ASTM procedure for porous bodies. Samples for density determination were taken from the middle of the gage length. After obtaining the weight of the sample in air, the pore openings in its surface were sealed by impregnation with liquid wax; the excess wax was wiped from the surface. The weight of the impregnated sample was then obtained in air and in water, the difference in the two being equal to the volume of the sample. The apparent density of the sample was calculated by dividing the weight (without wax) by the sample volume. Reproducibility of this method was estimated to be  $\pm 1$  per cent of the value of the density.

## 2.52 Metallographic preparation

. Samples taken from the specimen for metallographic inspection were mounted either in bakelite or in epoxy mixed with 0.3 micron alumina. Samples were mounted so that polishing exposed a section parallel to the cylindrical axis of the specimen. Mounting in bakelite was accomplished by the standard hot-pressing procedure. Mounting in alumina-dispersed epoxy was carried out in the following way. After blending the epoxy, 0.3 alumina powder was added in a 1 : 1 ratio by volume. The sample was placed in a hollow plastic cylinder sitting on its end on a glass plate. The cylinder was then filled to the desired level with the epoxy-alumina mixture and the entire assembly placed in a vacuum dessicator attached to a mechanical vacuum pump. The pressure on the system was reduced until the air within the porous sample



appeared to be removed. Pressure was then reapplied by opening the system to the atmosphere, thus forcing the liquid into the porous network of the sample. The alumina particles, due to agglomeration within the epoxy, did not make their way into the sample. However, their presence in the epoxy improved the abrasive qualities of the mount and helped to preserve the edges of the sample during polishing. The epoxy within the sample helped in preserving the true nature of the void-solid interface. For this reason, very low density specimens were usually mounted in the epoxy-alumina mixture; mounting in bakelite proved to be more efficient and adequate for intermediate and high density samples.

Mounted specimens were rough polished by hand on wet silicon carbide abrasive papers. Fine polishing was performed, in the sequential steps indicated below, on standard rotating-type polishing wheels covered with microcloths saturated with the following materials:

- (1) 600 grit silicon carbide particles and water,
- (2) 0.3 micron alumina and water, and
- (3) 0.25 micron diamond and lapping oil.

## 2.53 Metallographic examination

All specimens were metallographically examined without etching. Bausch and Lomb bench microscopes and metallograph were employed, depending on the magnification required, for all microscopy. The following quantitative metallography parameters were experimentally determined:

- (1)  $P_p$ ; the fraction of points of a grid, superimposed on the microstructure, which fall within the phase of interest, void or solid.
- (2)  $N_L$ ; the number of times a test line, superimposed on the microstructure, intercepts the void-solid interface, per unit length of test line.
- (3)  $T_{A_{net}} = T_{A_+} - T_{A_-}$ ;  $T_{A_+}$  and  $T_{A_-}$  are the number of tangents which occur between a test line swept across the microstructure and the convex\* and concave segments, respectively, of the void-solid interface, per unit area traversed by the sweeping test line.

The total length of test line employed in experimental measurement of  $N_L$  was determined by observation of the effect of accumulated length of test line on the accumulated average value of  $N_L$ . When the average value of  $N_L$  fluctuated no more than 5 per cent with further increase in total length of test line, this value was accepted. Experimental values of  $T_{A_{net}}$  were accepted when increase in total measured area caused no fluctuations greater than 10 per cent in the accumulated average value.

---

\* Throughout this work, convex (positive) segments of void-solid interface are those which are convex with respect to the solid phase.

## CHAPTER III

### EXPERIMENTAL RESULTS

#### 3.1 Sintering Force

Experimental values of the sintering force were determined as a function of density at three temperatures for copper powders with average particle diameters of 48, 30 and 12 microns. These data are compiled in Tables 1, 2 and 3 and presented in Figures 7, 8 and 9. For a given particle size the behavior of the sintering force with increasing density may be described as follows: in the first and second stages of densification the sintering force increases at a decreasing rate; this is followed by a sharp rise to a maximum value from which the sintering force decreases rapidly toward the zero value expected at the theoretical density of copper. This general functional dependence on density was obtained for each of the particle sizes; however, the maximum value appears to shift toward higher density with decreasing particle size.

Existence of the maximum value of the sintering force was verified by continuous measurement of the beam force which the specimen imposed upon itself (through shrinkage or creep in the direction of the applied load) as its density was increased primarily through radial shrinkage. In this way the force against which the specimen could shrink was clearly observed to pass through a maximum. Although the

Table 1. Experimental values of sintering force for the 48 micron particle size as a function of density and temperature

Final Density (gms/cm <sup>3</sup> )	Sintering Force (gms)	Test Temperature (°C)
5.75	25	950
5.78	23	950
5.80	24	950
5.90	28	950
5.98	31	950
6.57	38	1000
6.90	40	1000
7.02	35	1000
7.16	30	1050
7.26	48	1000
7.45	44	1000
7.55	38	1050
7.60	52	1050
7.60	48	1050
7.73	52	1050
8.18	75	950
8.20	65*	1050
	56	

\* Maximum (peak) sintering force.

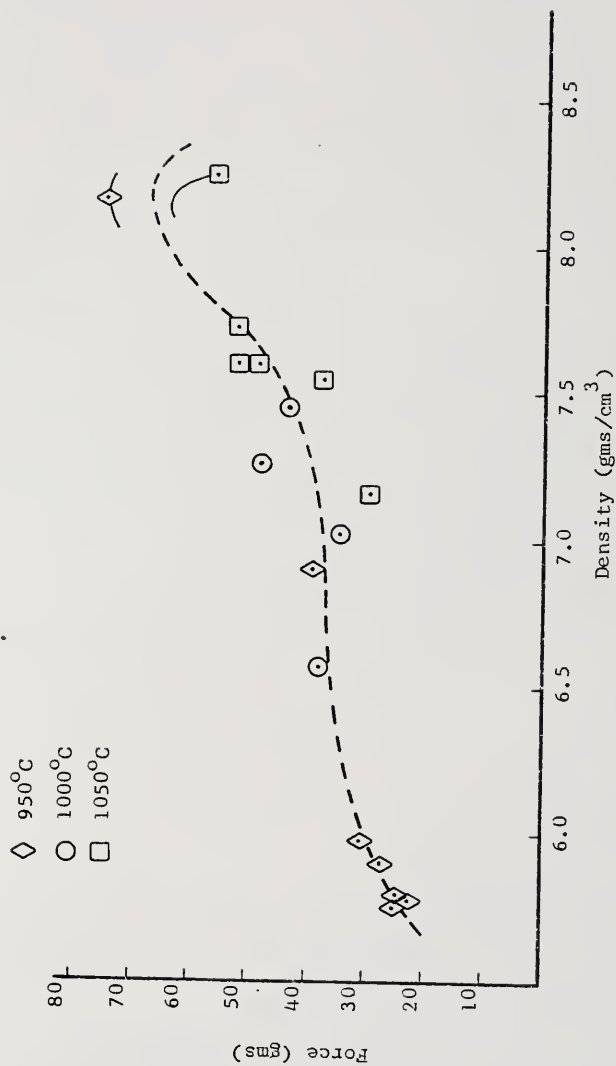


Table 2. Experimental values of sintering force for the 30 micron particle size as a function of density and temperature

Final Density (gms/cm <sup>3</sup> )	Sintering Force (gms)	Test Temperature (°C)
6.35	65	950
6.41	73	1000
6.48	79	1000
6.70	64	1000
6.78	91	1000
6.94	90	1000
6.95	100	1000
6.97	99	1000
7.19	95	1000
7.36	100	1000
7.46	110	1000
7.48	100	1000
7.53	95	1000
7.54	103	1000
7.86	120	1000
7.88	114	1000
7.93	90	1000
8.00	103	1000
8.10	108	950
8.20	112	1000
8.23	138*	1050
	129	
8.26	104	1000
8.37	147*	1050
	130	
8.40	145*	1050
	125	

\* Maximum (peak) sintering force.

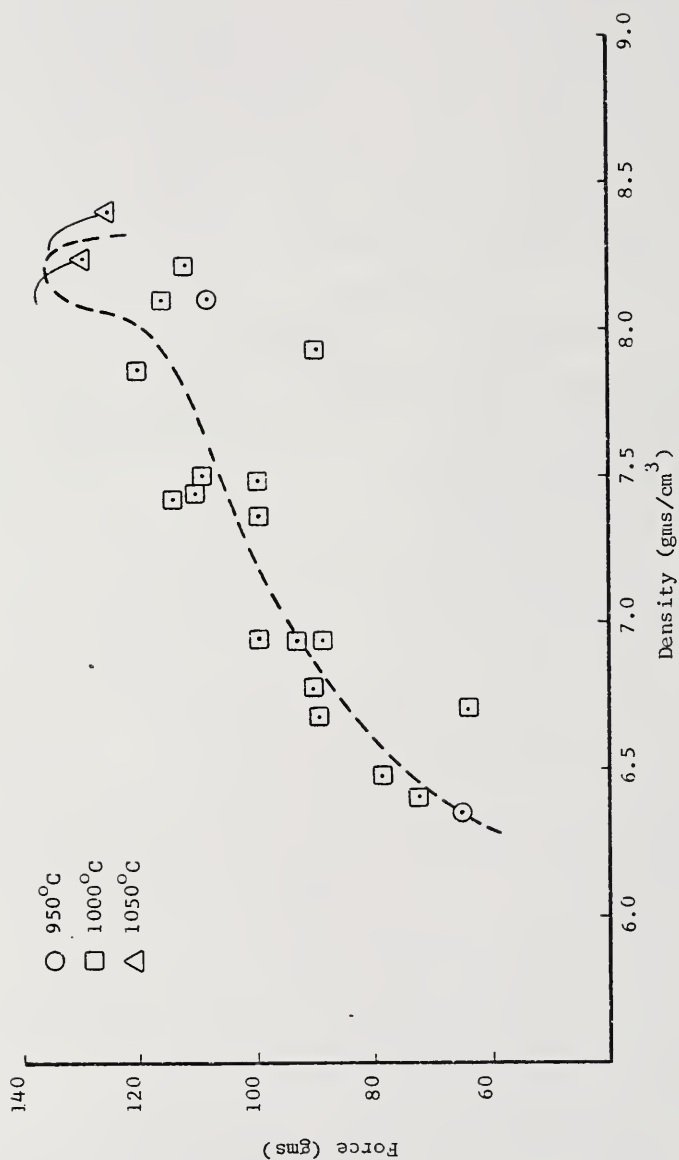


Figure 8. Experimental values of the sintering force as a function of density for the 30 micron particle size spherical copper powder. The solid lines indicate that the specimen corresponding to the data point passed through a maximum in sintering force.

Table 3. Experimental values of sintering force for the 12 micron particle size as a function of density and temperature

Final Density (gms/cm <sup>3</sup> )	Sintering Force (gms)	Test Temperature (°C)
6.16	89	1000
6.50	120	1000
6.59	126	1000
7.13	145	1000
7.26	150	1000
7.68	158	1000
7.71	155	950
7.82	154	950
8.17	176	1000
8.22	183	950
8.52	198* 182	1000
8.59	214* 203	1050
8.68	199* 192	1000

\* Maximum (peak) sintering force.



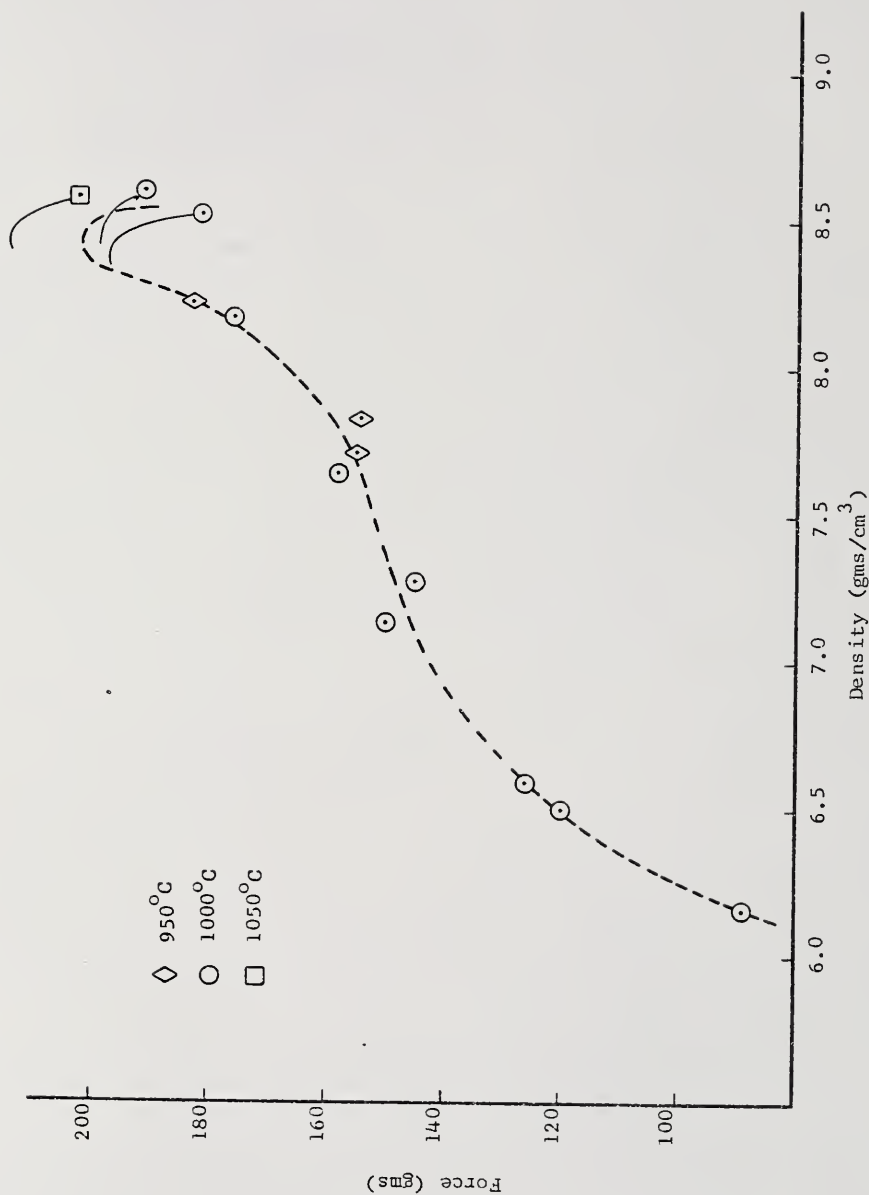


Figure 9. Experimental values of the sintering force as a function of density for the 12 micron particle size spherical copper powder. The solid lines indicate that the specimens corresponding to the data points passed through a maximum in sintering force.

evolution of the sintering force could be accurately measured by this procedure, only the final density of the specimen could be determined. Therefore, the lines drawn in Figures 7, 8 and 9 to indicate the behavior of the specimens in the region of the maximum sintering force are accurate with respect to force but estimated with respect to density. After the specimen had clearly passed through a maximum in sintering force, it was removed and its density determined. The data points at the ends of the lines drawn correspond to the final force and density.

Measurements of the sintering force were made at 950, 1000 and 1050°C. However, a complete documentation of the sintering force at each of these temperatures was not made since initial measurements revealed that the effect over this range of temperatures was negligible compared to the normal scatter of the experimental values. This knowledge was put to use in determination of the sintering force at high densities; the higher temperatures provided faster shrinkage rates and therefore greater sensitivity in the measurement of change in specimen length.

The lower limit in density at which measurement of the sintering force could be made was determined by the increase in density which the specimen achieved during the time (approximately 5 minutes) allowed for thermal equilibration of the load column after its insertion into the furnace. Consequently, the lowest density for which sintering force data were obtained increased with decreasing particle size.

### 3.2 Quantitative Metallography

The point count was used to calibrate the volume fraction of solid in the polished microstructure against the volume fraction predicted from the apparent density of the specimen. Polished specimens whose point count density was within  $\pm 2$  per cent of their apparent density were accepted for quantitative evaluation; those outside this limit were repolished.

Experimental values of  $N_L$  and  $T_{A_{net}}$  obtained from unetched microsections were used to calculate the surface area per unit volume,  $S_V$ , and the average value of mean curvature,  $\bar{H}$ , of the void-solid interface according to the relations

$$N_L = \frac{1}{2} S_V \quad (1)$$

and

$$\bar{H} = \pi \frac{T_{A_{net}}}{N_L} \quad (2)$$

$S_V$ ,  $\bar{H}$  and  $T_{A_{net}}$  data for the 48, 30 and 12 micron particle sizes are compiled in Tables 4, 5 and 6, respectively. They are plotted as a function of density in Figures 10, 11 and 12, and 14 through 19. Since  $N_L$  is simply related to  $S_V$ , it has been omitted from the tables and figures.

---

\* Mean curvature is defined by  $H = (\frac{1}{r_1} + \frac{1}{r_2})$ , where  $r_1$  and  $r_2$  are the principal normal radii of curvature. Its average value over the surface is defined [41] by  $\bar{H} = \frac{\iint H dS}{\iint dS}$ ; where the integration is performed over the surface,  $S$ .

Table 4. Quantitative metallography data for the 48 micron particle size as a function of density and temperature

Density (gms/cm <sup>3</sup> )	Temperature (°C)	S <sub>V</sub> (cm <sup>-1</sup> )	T <sub>A<sub>net</sub></sub> (cm <sup>-2</sup> × 10 <sup>-2</sup> )	$\bar{H}$ (cm <sup>-1</sup> )
5.90	950	458	340	466
5.98	950	520	225	272
6.57	1000	460	470	642
6.90	1000	362	545	946
7.02	1000	356	572	1010
7.16	1050	330	521	1011
7.55	1050	250	473	1189
7.60	1050	226	395	1098
7.60	1050	235	460	1230
7.73	1050	218	450	1297
8.18	950	137	320	1468

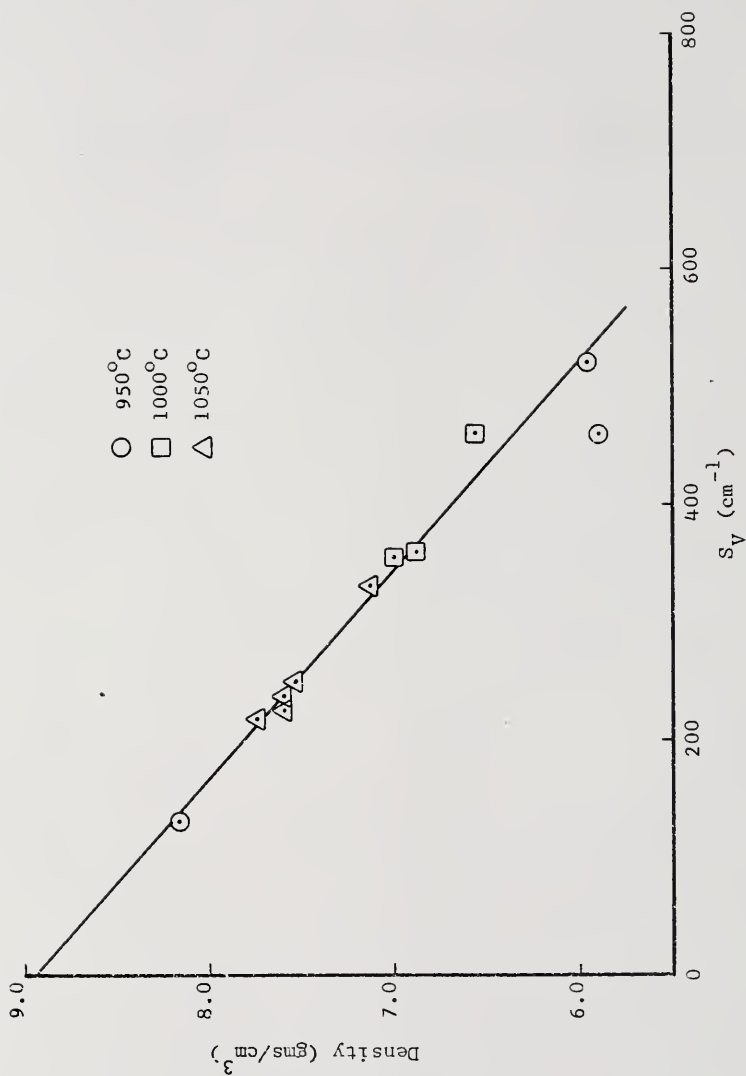


Figure 10. Variation of surface area per unit volume with density for the 48 micron particle size spherical copper powder.

Table 5. Quantitative metallography data for the 30 micron particle size as a function of density and temperature

Density (gms/cm <sup>3</sup> )	Temperature (°C)	S <sub>v</sub> (cm <sup>-1</sup> )	T <sub>Anet</sub> (cm <sup>-2</sup> × 10 <sup>-2</sup> )	$\bar{H}$ (cm <sup>-1</sup> )
6.48	1000	940	2520	1671
6.70	1000	860	2232	1631
6.94	1000	664	2793	2643
6.97	1000	830	2280	1726
7.36	1000	614	2710	2763
7.93	1000	366	1382	2373
8.00	1000	322	1604	3130
8.10	950	314	1206	2413
8.20	1000	230	1511	4128
8.23	1050	136	1192	5507
8.26	1000	248	896	2207
8.37	1050	164	1196	4582
8.40	1050	126	685	3416

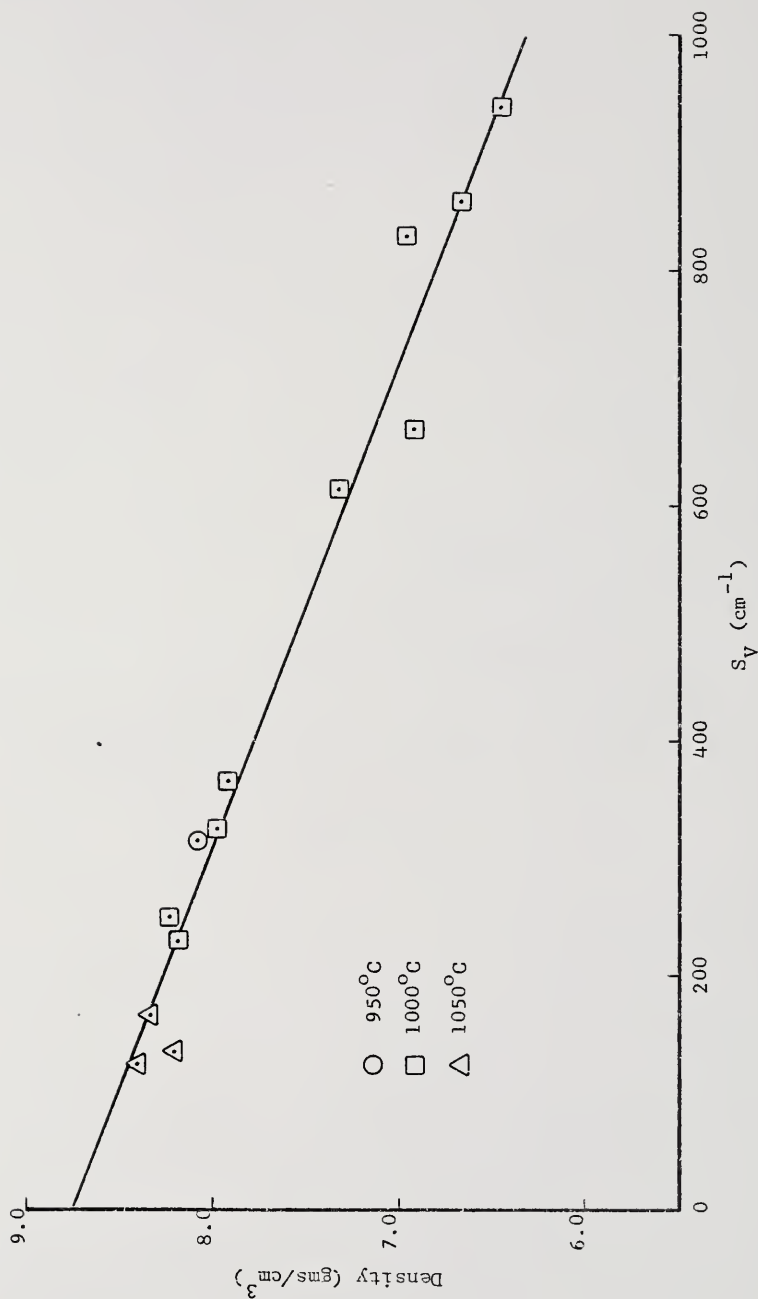


Figure 11. Variation of surface area per unit volume with density for the 30 micron particle size spherical copper powder.

Table 6. Quantitative metallography data for the 12 micron particle size as a function of density and temperature

Density (gms/cm <sup>3</sup> )	Temperature (°C)	S <sub>V</sub> (cm <sup>-1</sup> )	T <sub>Anet</sub> (cm <sup>-2</sup> × 10 <sup>-2</sup> )	$\bar{H}$ (cm <sup>-1</sup> )
6.16	1000	1778	2560	905
6.59	1000	1624	6570	2542
7.13	1000	1120	6080	3473
7.26	1000	1210	6190	3241
7.68	1000	744	3830	3234
7.82	950	740	4720	4008
8.17	1000	470	2960	3957
8.22	950	430	2550	3726
8.52	1000	214	2560	7576
8.59	1050	210	1420	4249
8.68	1000	122	930	4790



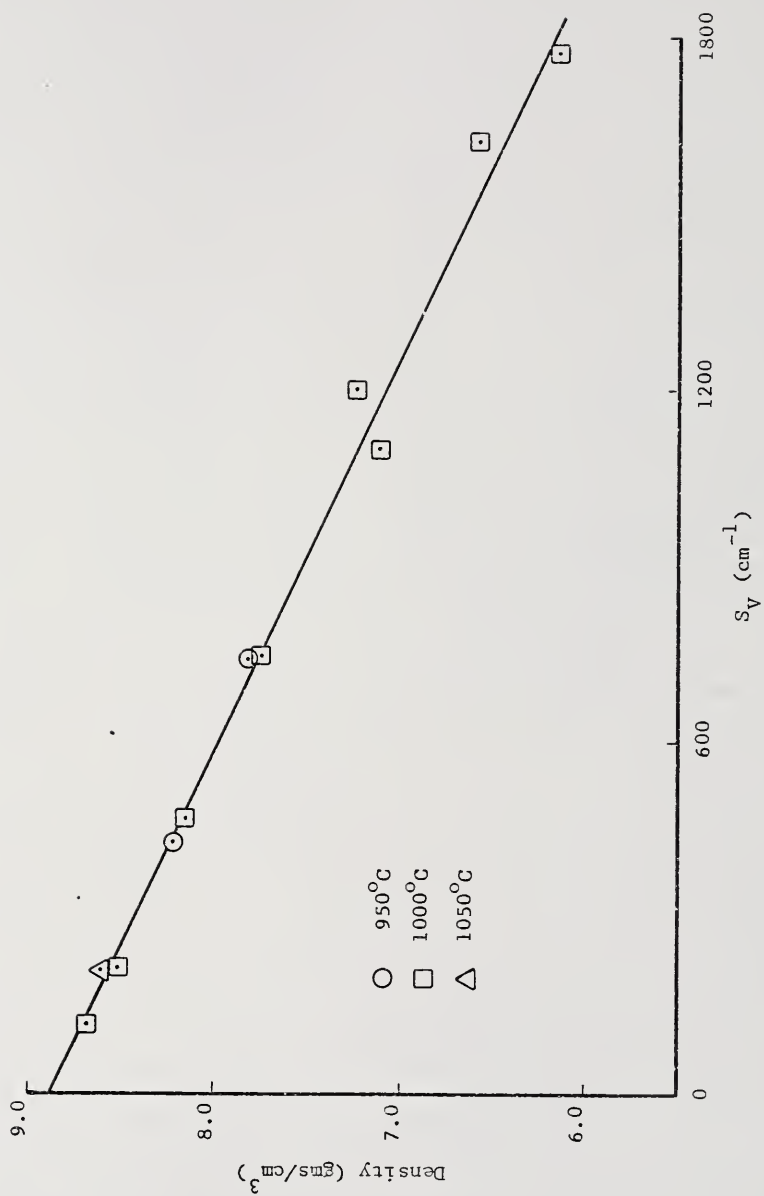


Figure 12. Variation of surface area per unit volume with density for the 12 micron particle size spherical copper powder.

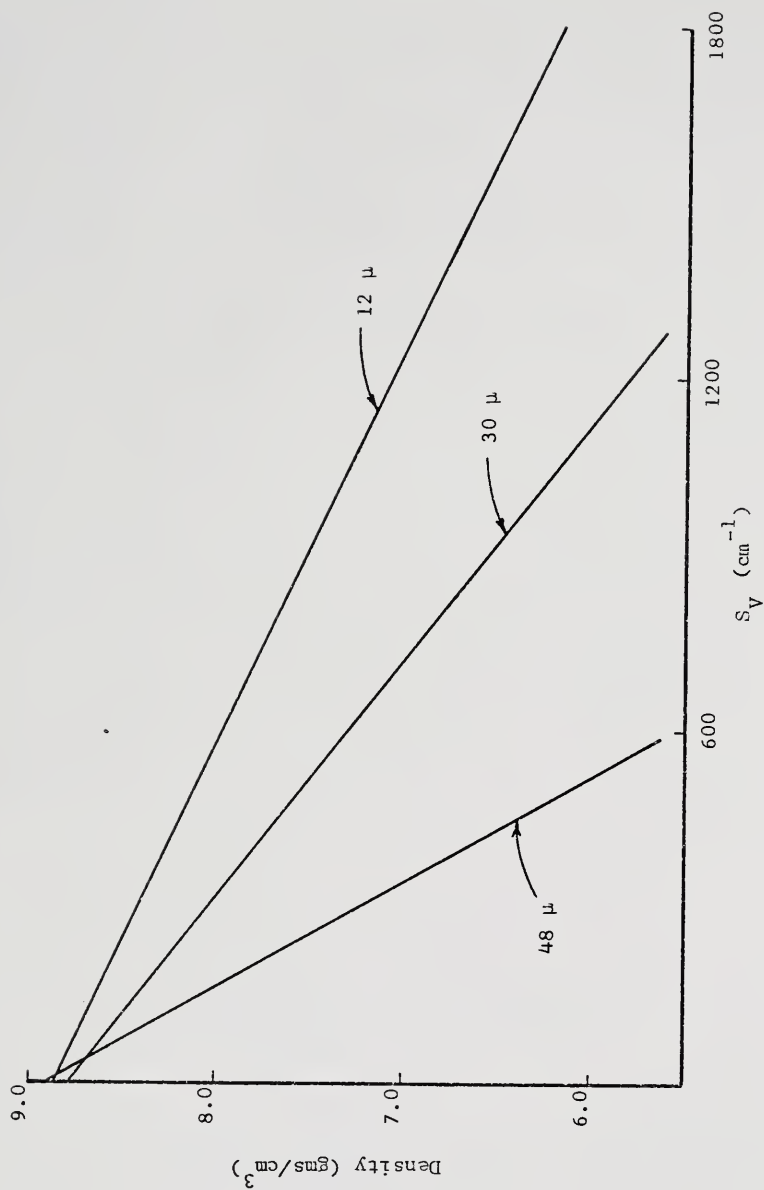


Figure 13. Comparison of the linear relationships between density and surface area per unit volume for the 48, 30 and 12 micron particle sizes.

### 3.21 Surface area of the void-solid interface

It is evident from Figures 10, 11 and 12 that the relationship between  $S_v$  and density is linear for each particle size. The lines drawn through the data for each particle size are presented for comparison in Figure 13. Their extrapolation to zero surface area produced reasonable agreement with the theoretical density of copper; maximum deviation was found for the 30 micron particle size for which extrapolation yielded a value of 8.8 gms per cm<sup>3</sup> as compared to the theoretical density of 8.94 gms per cm<sup>3</sup>.

The  $S_v$  data was collected from specimens sintered at each of the three test temperatures, 950, 1000 and 1050°C. The variation of temperature over this range had no effect on the surface area-density relationship.

### 3.22 Area tangent count

The algebraic sum,  $T_{A_{net}}$ , of the number of tangents per unit area with convex ( $T_{A+}$ ) and concave ( $T_{A-}$ ) segments of the void-solid interface, as determined as a function of density for the three particle sizes, is presented in Figures 14, 15 and 16. It is apparent that  $T_{A_{net}}$  was also insensitive to changes in test temperature.

For the loose stack of particles, all surfaces are convex (as previously defined) and  $T_{A_{net}}$  must therefore be positive. As contacts form between particles, concave elements are created and with the continued evolution of the geometry accompanying densification  $T_{A_{net}}$  passes through zero and becomes negative. As evidenced by Figures 14, 15 and 16,  $T_{A_{net}}$  was found to be negative over the entire range of densities for which the sintering force was determined. The functional dependence

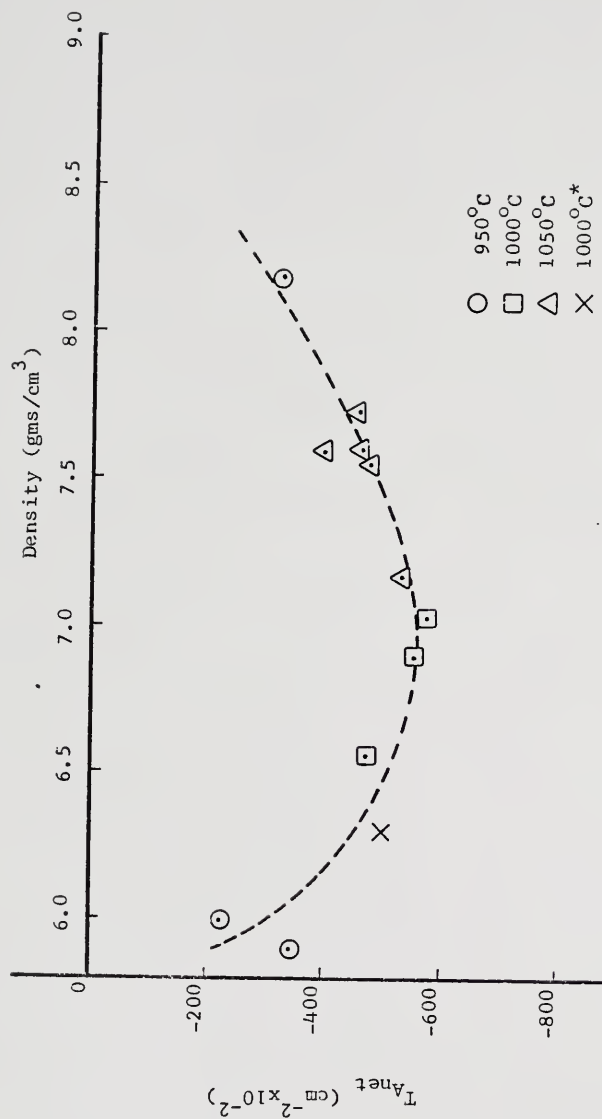


Figure 14. Variation of the net area tangent count with density for the 48 micron particle size spherical copper powder. (\*Obtained from specimen sintered without external constraint.)

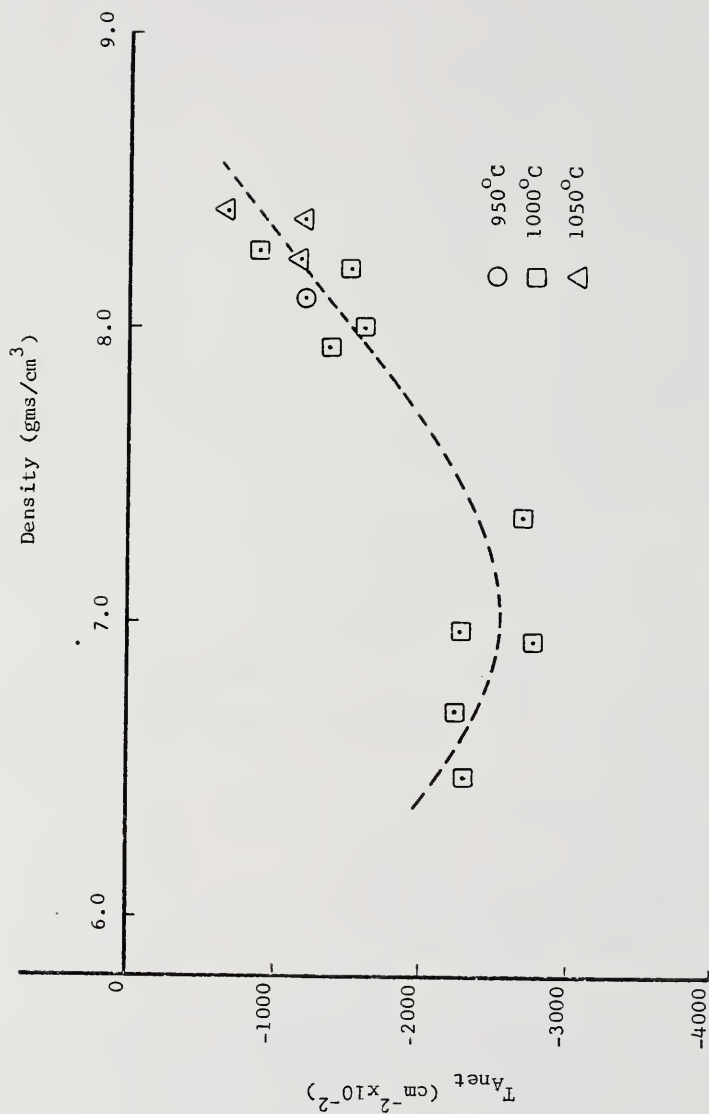


Figure 15. Variation of the net area tangent count with density for the 30 micron particle size spherical copper powder.

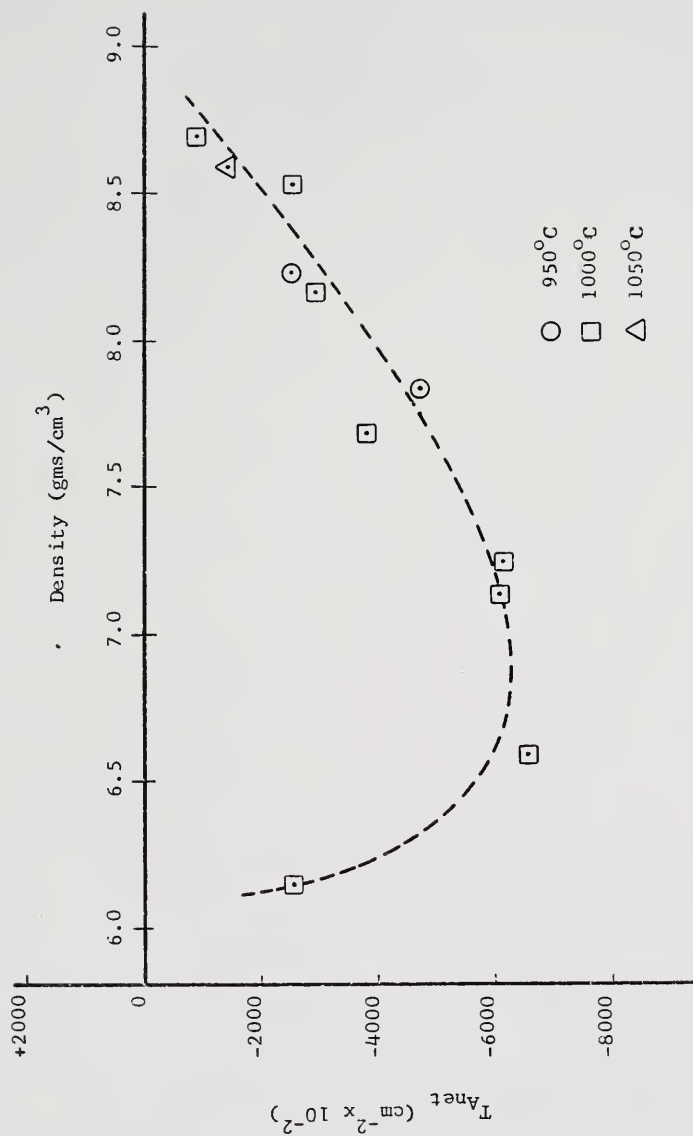


Figure 16. Variation of the net area tangent count with density for the 12 micron particle size spherical copper powder.

of  $T_{A_{net}}$  on density was similar for each particle size; increasing to a maximum (negative) value in the region of 75 - 80 per cent of theoretical density and then decreasing toward the zero value which must exist when densification is complete.

### 3.23 Average mean surface curvature

Average values of the mean surface curvature,  $\bar{H}$ , are presented in Figures 17, 18 and 19 for the 48, 30 and 12 micron particle sizes, respectively. Since  $\bar{H}$  derives its sign from  $T_{A_{net}}$ , the average values of the mean surface curvature were also negative for all sintering force specimens. In addition, since  $N_L$  and  $T_{A_{net}}$  were used to calculate  $\bar{H}$ ,  $\bar{H}$  was also insensitive to changes in test temperature. The general shape of the curve depicting the mean surface curvature-density relationship indicates that  $\bar{H}$  progresses from positive to negative values in the region of 65 - 70 per cent of theoretical density (approximately 6.0 gms/cm<sup>3</sup>). The similarities between the functional dependence of  $\bar{H}$  on density and that exhibited by the sintering force (in Figures 7, 8 and 9) are striking and a most significant discovery in terms of the relationship between the microstructure of a sinter body and its sintering behavior. Further elaboration of this point may be found in Chapter IV.

### 3.24 Effect of uniaxial constraint on sintering behavior

It was reasonably expected that the effect of uniaxial loading on a sinter body, attempting to shrink isotropically, would distort the microstructure of the specimen and in so doing produce artificial behavior in the development of the geometric properties. Indeed, it was

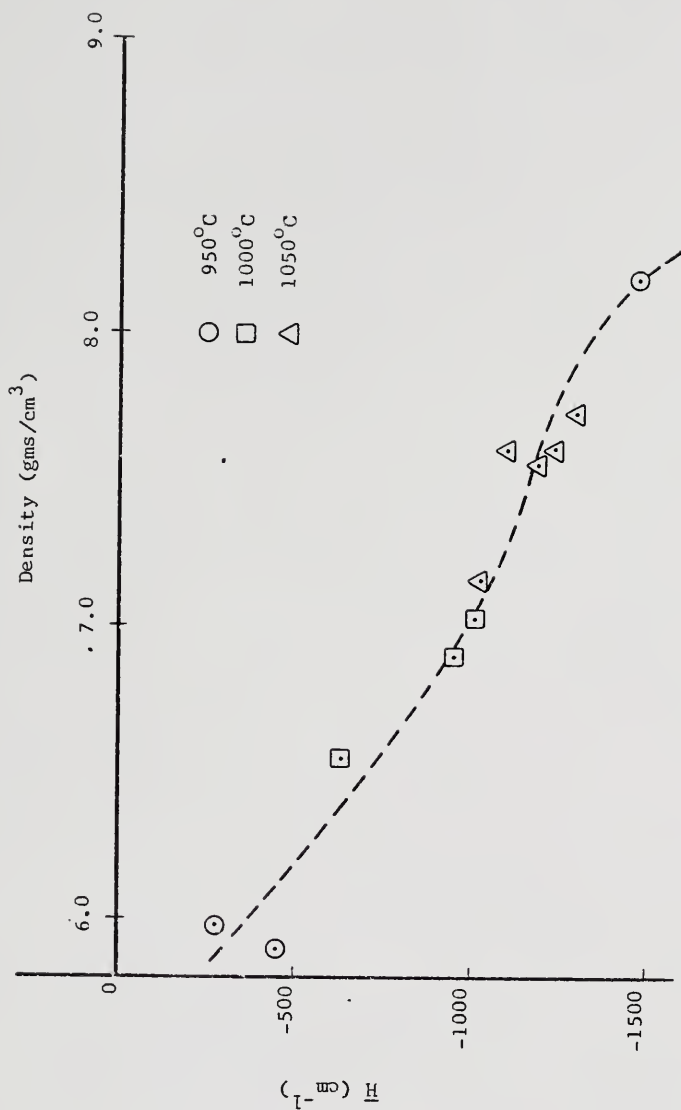


Figure 17. Variation of the average mean curvature of the void-solid interface with density for the 48 micron particle size spherical copper powder.



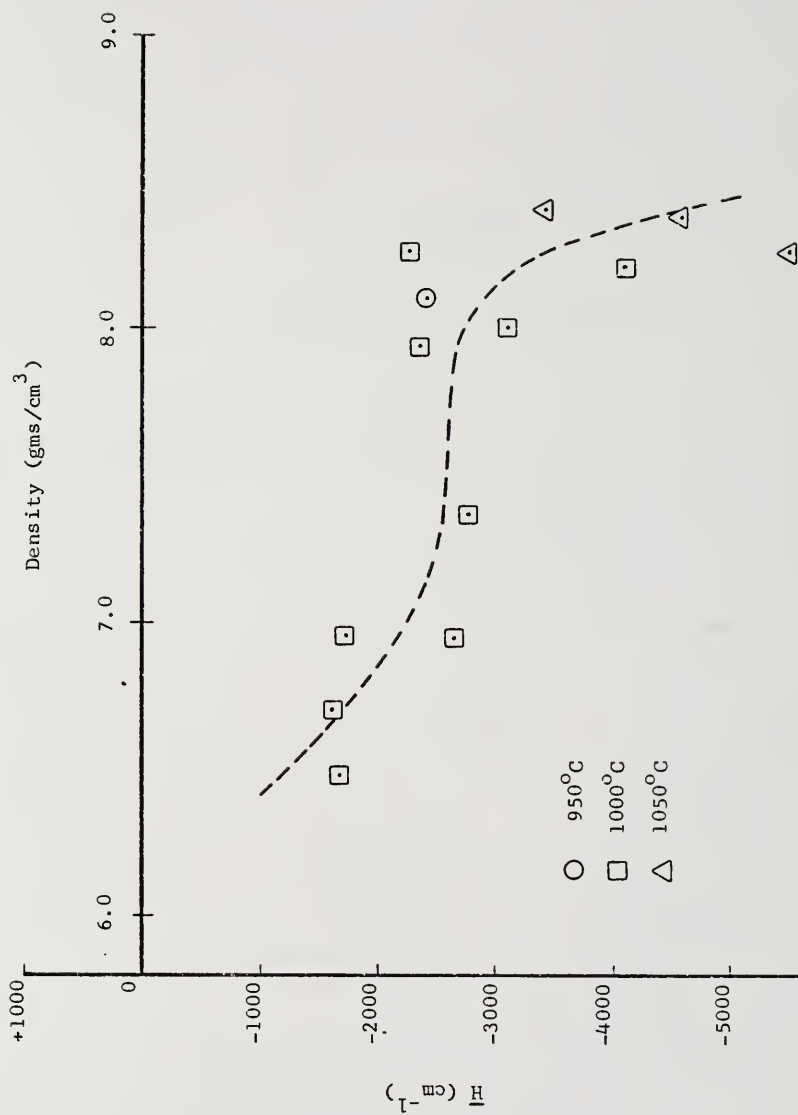


Figure 18. Variation of the average mean curvature of the void-solid interface with density for the 30 micron particle size spherical copper powder.

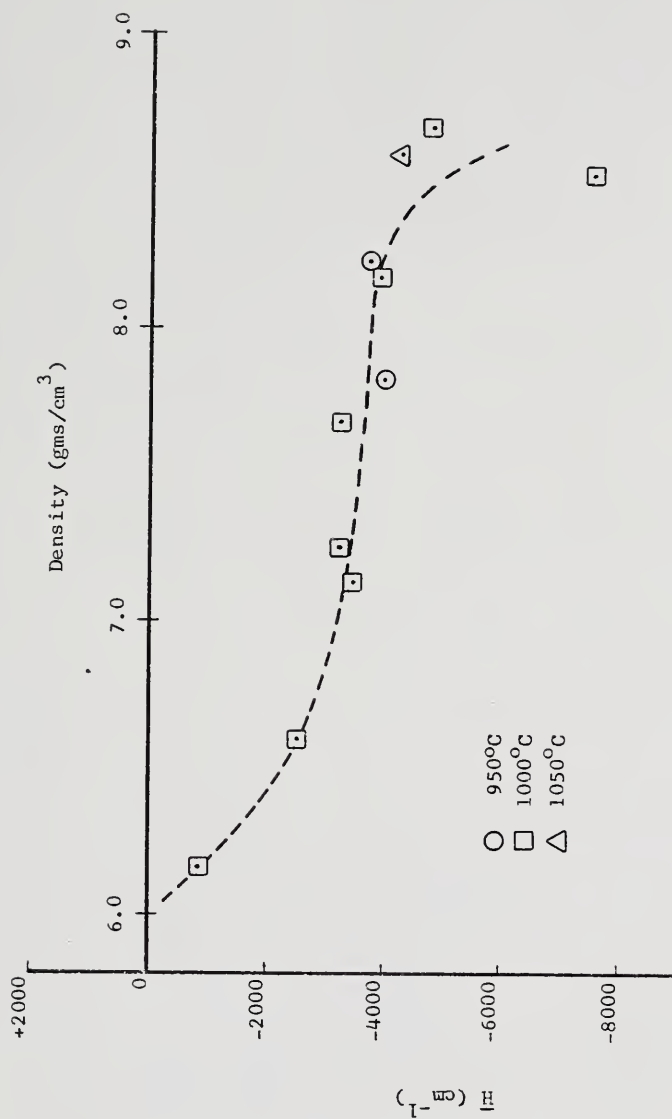


Figure 19. Variation of the average mean curvature of the void-solid interface with density for the 12 micron particle size spherical copper powder.

observed, in the very beginning of this research, that extreme overloading above the force against which the specimen could shrink produced internal necking and severe distortions of the void-solid interface. However, as long as the overload was maintained close to the minimum needed to produce creep of the specimen, it was impossible to detect any effect of the external load on the geometric development of the microstructure. The veracity of this statement has been experimentally substantiated. For example,  $N_L$  measurements which were made parallel with, perpendicular to and at a  $45^\circ$  angle to the direction of external load revealed no statistically significant differences from the values measured without respect to specimen orientation. In addition, the slopes of the  $S_V$ -density plots (see Figure 13) were found to correlate with the average particle diameter in the same way as previously reported by DeHoff et al. [38] for unconstrained sinterings made from the same powder material; this correlation is presented in Figure 20.

In Figure 21, the cross-sectional areas calculated from the diameters of the specimen after testing are presented as a function of density. The upper boundary in the figure represents the cross-sectional area which would develop during unconstrained (isotropic) shrinkage. The lower boundary is that predicted by assuming that external constraint is applied in a fashion which limits all shrinkage to the radial directions of the cylindrical specimen. Essentially all specimens fall within these boundaries, indicating that the overloading of the specimens used either initially in straightening the specimen in the load column or in determination of the balance point between

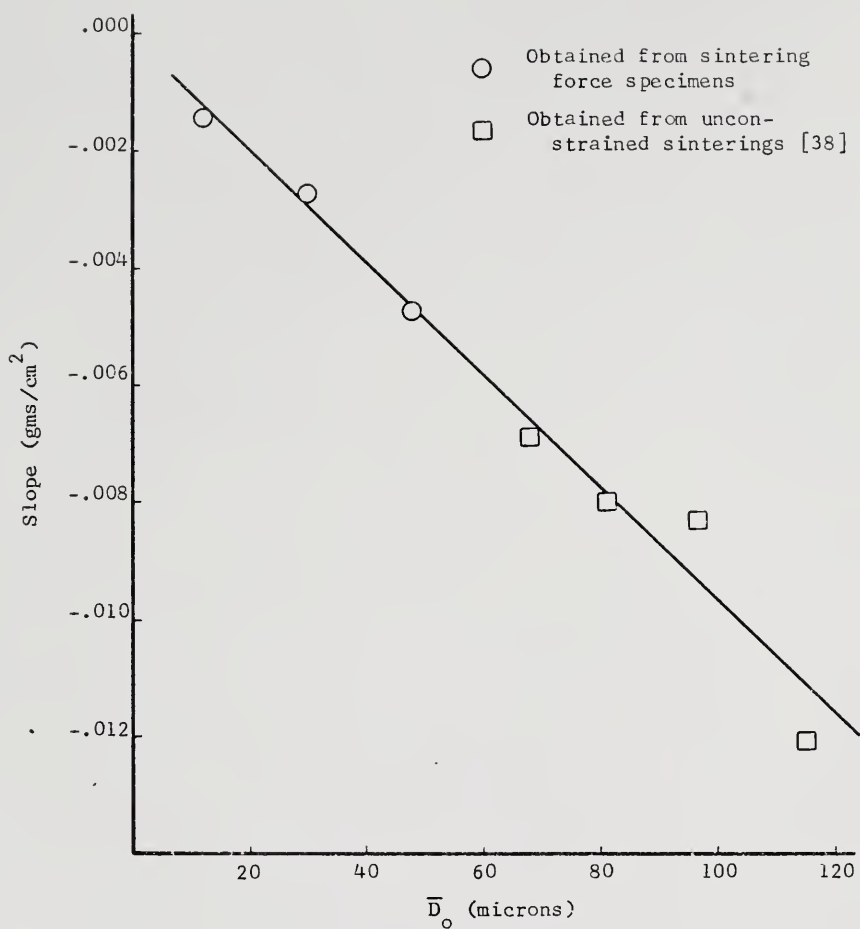


Figure 20. Correlation of the slope of the surface area-density relationship with initial particle size for spherical copper powder.

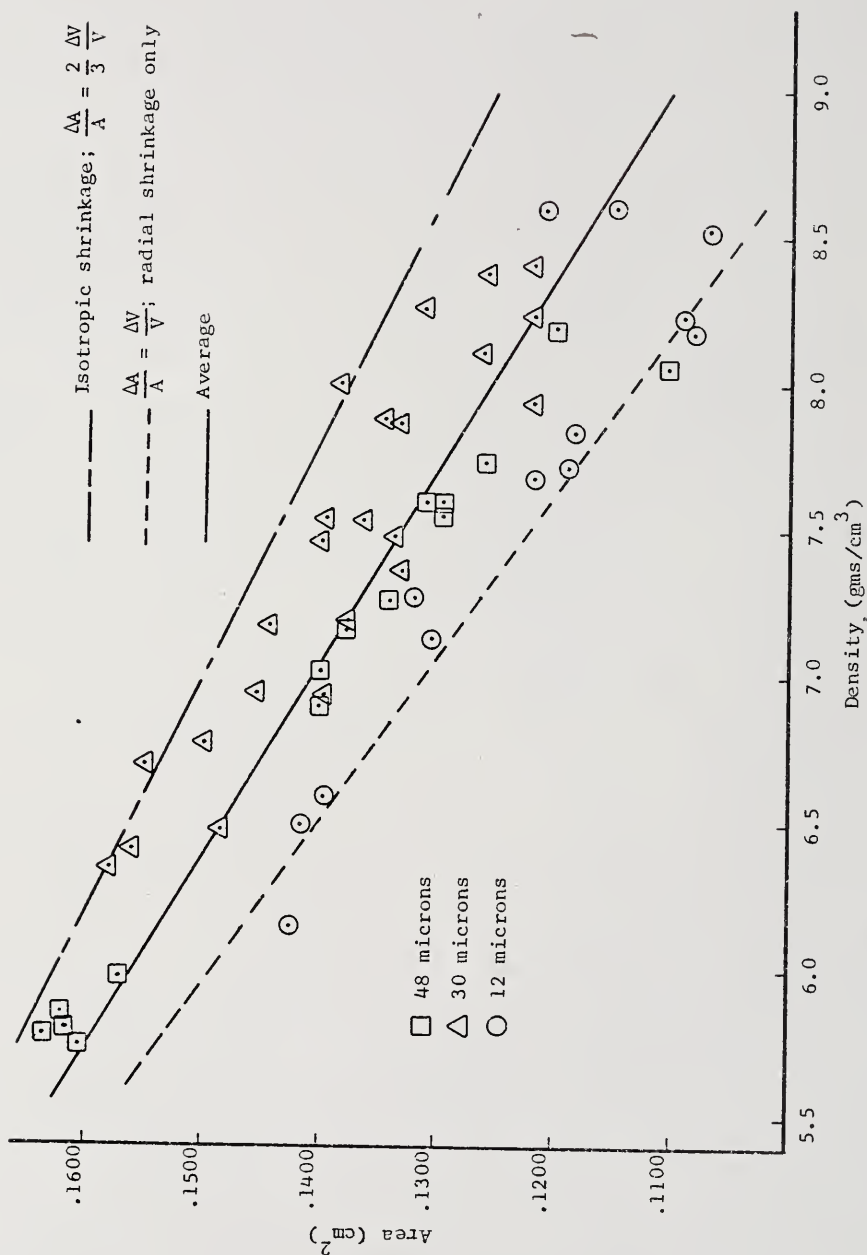


Figure 21. Cross-sectional areas of sintering force specimens after testing. The areas predicted by isotropic shrinkage lie on the upper boundary; those which should result from radial shrinkage only lie on the lower boundary.

elongation and shrinkage, did not unduly distort the specimen macroscopically. The scatter in the cross-sectional areas was produced by variations in the fraction of the total time at temperature during which the specimens were under external constraint.

## CHAPTER IV

### DISCUSSION

The results of this investigation have revealed the sintering force to be an experimentally measurable and reproducible property whose functional dependence on density, particle size and temperature are consistent with and relatable to the geometric evolution of the sintered structure. To analyze these results, it is necessary to consider the general relationships between surface geometry and surface tension forces and the details of the geometric evolution of the void-solid interface during densification. A method for estimating the magnitude of the surface tension forces in a sinter body will be formulated from these considerations and compared with experimental values of the sintering force.

The ultimate objective of this research was to establish, through the concept of the sintering force, a relationship between the microstructure of the sinter body and its sintering kinetics. Sensitivity of the rate of sintering to the geometry of the microstructure will be demonstrated through the conjoint application of an empirical treatment of the mechanical behavior of the sinter body and a stress-strain rate relation based on deformation by creep.

#### 4.1 Surface Energy and Surface Tension of Solids

Specific surface energy,  $\gamma$ , is defined as the energy necessary to increase the surface by unit area, and has units of energy per unit area. Surface tension,  $\sigma$ , is the force which resists stretching of the surface; it has units of force per unit length and may be considered to act in the surface, perpendicular to any line drawn in the surface. The equality of surface energy and surface tension in liquids has been documented by many experiments in liquid capillarity. Gibbs [49], in his rigorous formulation of the thermodynamics of interfaces, pointed out that this equality does not always exist in solid surfaces. Shuttleworth [50] has developed a general relationship between surface energy and surface tension which reveals the conditions under which these two surface properties have the same magnitude. This relationship may be developed, following Shuttleworth's arguments, in the following way. Imagine a crystal surface cut by a plane perpendicular to it and penetrating only a short depth below the surface. To maintain the surface on both sides of the cut in equilibrium, it is necessary to apply, in the plane of the surface, equal and opposite forces to each side of the cut. For anisotropic surfaces, the total force per unit length of the cut is defined as a surface stress which may vary with the orientation of the cut with respect to the atomic arrangement of the crystal surface. Consider the deformations  $dA_1$  and  $dA_2$  of the segment A of the solid surface in Figure 22, by forces working against the surface stresses  $\sigma_1$  and  $\sigma_2$ . If these deformations are performed reversibly and isothermally, then the work done against the surface



stresses will be equal to the increase in the total (Helmholtz) free energy,\*

$$\sigma_1 dA_1 + \sigma_2 dA_2 = d(A\gamma) \quad (3)$$

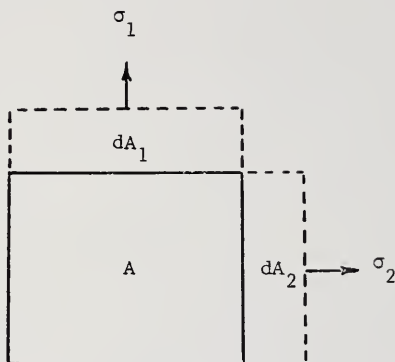


Figure 22. Schematic of surface stresses in a solid.

In the absence of surface anisotropy, as in a liquid, the surface stresses,  $\sigma_1$  and  $\sigma_2$ , are equivalent and may be considered as a single value, a surface tension, which characterizes the surface. Under these conditions equation (1) reduces to

$$\sigma = \gamma + A\left(\frac{d\gamma}{dA}\right) \quad (4)$$

---

\* For a unary system, at constant temperature and volume, in which  $\gamma$  is independent of changes in area,  $\gamma = dF/dA$ , where  $F$  is the Helmholtz free energy. For systems in which  $\gamma$  is a function of area, the total change in free energy will be  $d(\gamma A)$ .

In the deformation of any surface, liquid or solid, where the mobility of the atoms or molecules is sufficiently high to maintain the original surface density of atoms or molecules throughout the deformation,  $(\frac{dy}{dA})$  will be zero, and surface tension and surface energy will be equivalent in magnitude. In liquids, this mobility is easily obtained; in solids, it may be reasonably assumed that the conditions required exist during slow deformation of surfaces at temperatures close to the melting point where atomic mobility is high. Since these conditions were satisfied by the testing procedure in this research, it has been assumed that surface energy and surface tension are equivalent in magnitude. In keeping with this assumption, the symbol for surface energy,  $\gamma$ , has been used interchangeably for surface tension and surface energy. In addition, it has been assumed that the random, polycrystalline nature of the sintered structure assures a statistical distribution of all orientations of the crystal surfaces at the void-solid interface which obviates any corrections for anisotropy of surface tension.

#### 4.11 Pressure difference across a curved surface

It has been demonstrated that for a surface of zero curvature, the surface tension can be balanced by applying external forces parallel to the surface at its periphery. The experimental application of this principle will be discussed in the next section. However, for curved surfaces, surface tension forces result in pressures normal to each point of the surface. The magnitude of this normal pressure may be related to the local curvature of the surface in the following way. Consider the square segment of surface shown in Figure 23, with

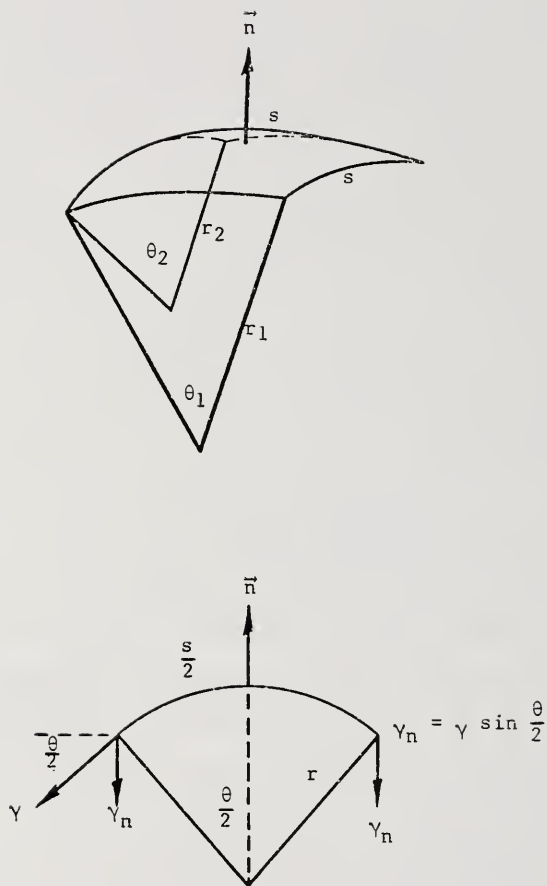


Figure 23. Resolution of surface tension into a pressure acting normal to each point of a curved surface.

sides of arc length  $s$  and normal radii of curvature  $r_1$  and  $r_2$ . From the edge view it is apparent that the components of surface tension parallel to the surface normal are equal on opposite sides of the element. If the element is extremely small, then  $\sin \frac{\theta}{2}$  is approximately equal to  $\frac{\theta}{2}$ , and the forces have total components (parallel to the surface normal) of  $\frac{\gamma s^2}{r_1}$  and  $\frac{\gamma s^2}{r_2}$ . The difference in pressure,  $\Delta P$ , between the volumes separated by the surface is the normal pressure at each point of the surface. The normal component of force resulting from this pressure is  $\Delta P s^2$ . Therefore, the condition for mechanical equilibrium of the surface is

$$\Delta P = \gamma \left( \frac{1}{r_1} + \frac{1}{r_2} \right) \quad (5)$$

Thus, the effect of surface tension on an arbitrarily curved segment of surface can be analyzed in terms of the geometry of the surface.

#### 4.12 Measurement of surface tension effects in solids

Surface forces are small in magnitude and are negligible when compared to the loads required to overcome the elastic strength of solids at normal temperatures. However, as discussed above, their effects become noticeable at high temperatures. The effect of surface tension in solids was first reported by Faraday [51] who observed that thin metal sheets would shrink when heated. However, it remained for Chapman and Porter [52] to attribute this effect to the presence of forces in the metal surface. Schottky [53], Sawai and Nishida [54] and Tammann and Boehme [55] were among the first to use the shrinkage of metal foils to determine values of surface tension.

They employed the method, originally suggested by Gibbs [49], of opposing the shrinkage of the foil with known external forces. More recently, Udin et al. [12] measured the surface tension of copper by determining the external load required to stop the shrinkage of fine wires. Since the sintering force, as defined in this research, embodies the same principle of a balance of forces it is appropriate to consider the analyses of the foil and wire experiments.

The mechanical conditions for balancing the shrinkage of foils with external loads have been reviewed by Fisher and Dunn [56]. The simplest geometrical arrangement for balancing the surface tension of a foil is presented in Figure 24(a). The top and vertical sides of the foil are constrained while the remaining edge is free. However, the two vertical sides of the foil are allowed to slide up and down without friction. If the thickness,  $t$ , of the foil is neglected, the external load which just balances the surface tension forces may be calculated from the relation

$$F = 2\gamma w \quad (6)$$

where  $\gamma$  is the specific surface energy (tension) and  $w$  is the foil width. However, these experimental conditions cannot be achieved. Figure 24(b) shows the more accessible situation in which the vertical sides are also free. In this condition the horizontal shrinkage of the foil will contribute to the length changes in the vertical direction and requires a different analysis. If it is assumed that a condition of plane stress exists, then the stresses in the foil are

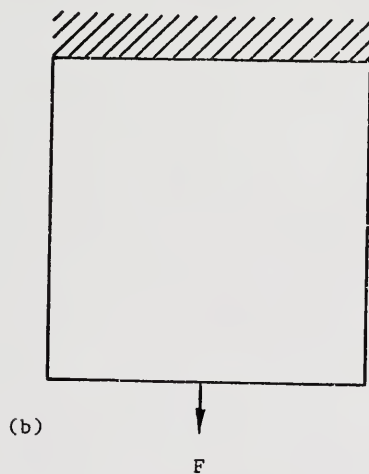
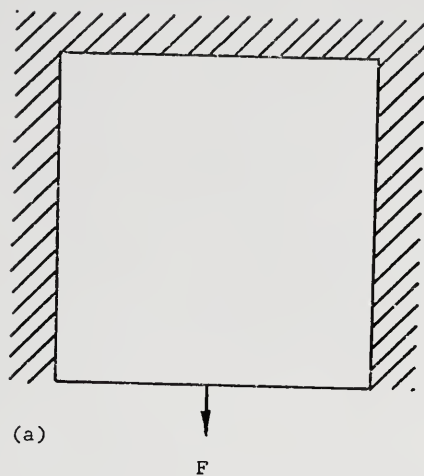


Figure 24. Two arrangements for balancing the shrinkage of metal foils by inducing creep with an external force.

$$\sigma_v = \frac{F - 2\gamma w}{wt}$$

and

(7)

$$\sigma_h = \frac{2\gamma}{t}$$

where  $\sigma_v$  and  $\sigma_h$  refer to the vertical and horizontal directions, respectively. Plastic strain in the vertical direction may be estimated by

$$\epsilon_v = \frac{1}{E_p} \left[ \sigma_v - \frac{1}{2}(\sigma_h) \right] \quad (8)$$

where  $E_p$  is the plastic modulus and Poisson's ratio has been assumed to be 1/2. If it also assumed that the strain rate,  $\dot{\epsilon}_v$ , in the vertical direction is proportional to the stresses producing strain in this direction, then the stress state for  $\dot{\epsilon}_v = 0$  under external load is

$$\sigma_v = \frac{1}{2} \sigma_h \quad (9)$$

which, on substitution, reduces to

$$F = \gamma w \quad (10)$$

For the circular cross section wire used by Udin et al. [12] the same principles apply; however, the stress state is now three-dimensional. For zero longitudinal strain rate in the wire, the assumption of constant volume results in zero radial strain rate. These conditions are consistent with the existence of a hydrostatic stress state. Therefore, the conditions for balance under the external force are

$$\sigma_l = \frac{F - 2\pi r\gamma}{\pi r} = \sigma_r = -\frac{\gamma}{r} \quad (11)$$

or

$$F = \pi r \gamma \quad (12)$$

where  $r$  is the radius of the wire cross section, and  $\sigma_l$  and  $\sigma_r$  are the longitudinal and radial stresses, respectively. Udin [57] corrected equation (12) by deriving a new relationship based on the energetics of the process. Included in this analysis was the effect of grain boundaries within the wire. As shown in Figure 25, the grain boundaries were aligned perpendicular to the cylindrical axis of the wire in a configuration referred to as "bamboo" structure. For a reversible process, the change in potential energy of the external load must be balanced by the total energy change in the wire. If the latter is composed only of changes in grain boundary and external surface area, then

$$F dl = \gamma dA + \gamma' dA' \quad (13)$$

where the prime notation refers to the grain boundaries. If it is assumed that the changes in length and radius of the wire are related by a Poisson's ratio of  $1/2$ , equation (13) becomes

$$F = \pi r \gamma - n \pi r^2 \gamma' \quad (14)$$

where  $n$  is the number of grain boundaries per unit length of the wire. The grain boundary effect in Udin's data changed the experimental value of the surface tension of copper at  $1000^\circ\text{C}$  from 1430 to 1670 dynes per cm; an increase of approximately 17 per cent. The use of foil geometry has been criticized due to its complicated grain boundary configuration and the assumptions required to analyze its state of



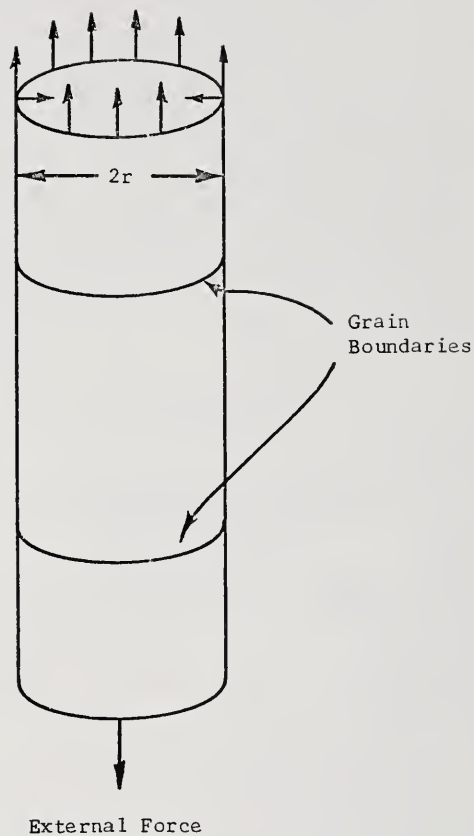


Figure 25. Schematic of surface tension forces and grain boundary array in wire geometry used for determination of surface tension in metals.

stress. The few values of the surface tension of metals which have received general acceptance have been determined from the wire geometry.

It has been demonstrated that the effect of surface tension forces in solids can be experimentally analyzed through knowledge of the geometry of the surface. The shape of the void-solid interface in a sinter body is extremely complex; consequently, it is necessary to develop some understanding of its geometry before attempting to analyze the surface tension forces which exist within it. The analysis which will then be developed will not include an effect of grain boundaries. It has been assumed that the effect of grain boundaries on the experimental values of the sintering force is subordinate to the effect of the void-solid interface and within the scatter of the experimental results. This assumption is based on preliminary measurement of the ratio of grain boundary to void-solid surface area in the specimens used in this investigation [58], and also consideration of the fact that the energy of grain boundaries in copper is approximately  $1/3$  of the energy of a free copper surface [59].

#### 4.2 The Geometry of Sintering

The degree to which one may describe the complex structural changes in a three-dimensional sinter body, which occur during its progression from a loose particle stack toward complete densification, has been summarized by DeHoff and Rhines [60]. They pointed out that it is now possible to determine experimentally the following geometric parameters of a sintered structure:

- (1) total void volume,
- (2) total area of the void-solid interface,
- (3) average mean curvature of the total void-solid interface [41] (see Appendix II),
- (4) connectivity of the pore network (expressed as the genus of the void-solid interface, (see Appendix I), and
- (5) the number of separate parts of the void volume.

The first three of these parameters are sensitive to the dimensions of the system; the last two are topological parameters, insensitive to dimension but necessary to characterize the topological shape of the system. Experimental evaluation of these parameters has enabled Rhines and DeHoff to deduce a reasonably complete and comprehensive description of the structural evolution of a sintering system.

The application of descriptive topology, as developed by Rhines [1], separates the structural evolution into three stages. These separations are based on the variation in connectivity of the void phase with increasing density. Experimental evaluation of this parameter for the 48 micron copper powder [60] is presented in Figure 26. The formation and growth of interparticle contacts constitutes the first stage of sintering. In this stage the independent processes of surface rounding (primarily by surface or vapor transport) and shrinkage should proceed without affecting the connectivity of the pore network. However, as evident in Figure 26, the connectivity increases during the first stage. This behavior is the result of the formation of "bridges" in the loose particle stack. Particles in these regions, originally not in contact, are brought together by the shrinkage of the particle

framework, thereby increasing the total connectivity of the void phase. The contributions to the decrease in total surface area by surface and vapor transport, and by shrinkage, continue to be independent until the minimal surface area is achieved for the existing values of volume and connectivity of the void phase; this signals the end of the first stage. Further decrease in surface area requires a new set of values of connectivity and total pore volume. Rhines (see Appendix I) has demonstrated that the system can progress to lower values of the minimal surface area through continual decreases in the connectivity of the void volume. There exist two experimental findings which support the minimal area concept in the second stage. First, the relation between the density of the system and the surface area it contains in unit volume is linear throughout the second stage. Second, the onset of this linear relation coincides with the beginning of a strictly monotonic decrease in the connectivity of the pore network with increasing density; as shown in Figure 26. This decrease in connectivity is produced by closure of the channels in the multiply-connected void volume. The criterion for closure of a channel, in terms of local instability of the void-solid interface, is revealed to a degree by the linear relationship between the density and surface area per unit volume; DeHoff and Rhines [60] have concluded that this behavior is indicative of channel closure events which remove elements of the void phase having a fixed ratio of volume to associated surface area. This conclusion is consistent with their previous finding [38] of a constant

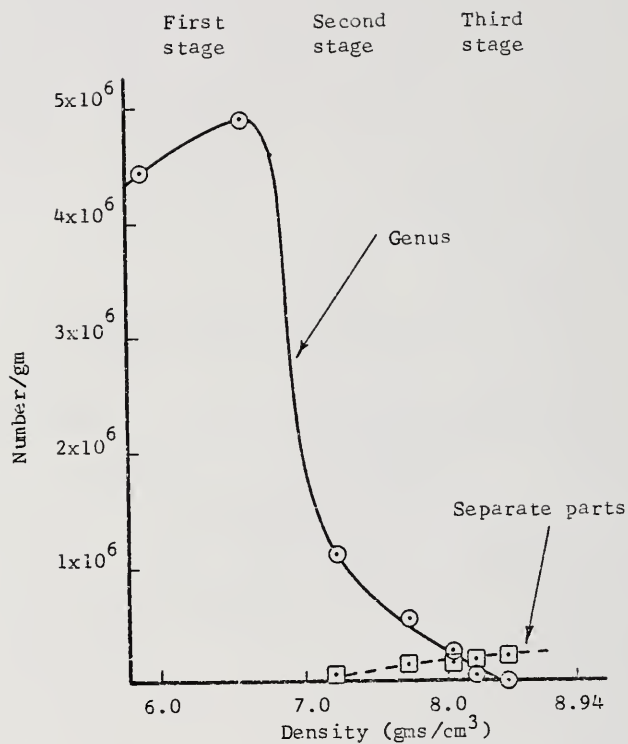


Figure 26. Variation of genus (connectivity) and number of separate parts of the void-solid interface with density for the 48 micron special copper powder [43].

value of the mean lineal intercept<sup>\*</sup> of porosity in the second stage of sintering. Channel closure continues to be the dominant structural change throughout the second stage. Eventually the pore network is no longer multiply connected and the genus is then equal to zero. In the third stage, the number of separate parts of the void volume is increased through further division of the complex but simply-connected "tree-like" [60] cavities by channel closure. The number of separate parts decreases from the maximum value primarily through a reduction in number resulting from conglomeration with other portions of the void volume.

#### 4.21 The evolution of curvature of the void-solid interface

To determine the relationship between the surface tension forces and the microstructure of the sinter body, it is necessary to consider the information available on the evolution of the curvature of the void-solid interface. Constant reference by the reader to Figure 26, which depicts the three stages of sintering and to Figure 27, a compilation of the average mean curvature values,  $\bar{H}$ , for the three particle sizes used in this investigation will serve to clarify the following discussion.

In the initial loose stack of particles, the curvature of all void-solid interfaces is positive, by definition. The average value of

---

<sup>\*</sup> Mean lineal intercept,  $\bar{\lambda}$ , is the average length of all lines traversing the phase of interest and is calculable from Fullman's [61] relation,  $\bar{\lambda} = 4 \frac{V_V}{S_V}$ ; where  $V_V$  and  $S_V$  pertain to the phase of interest.

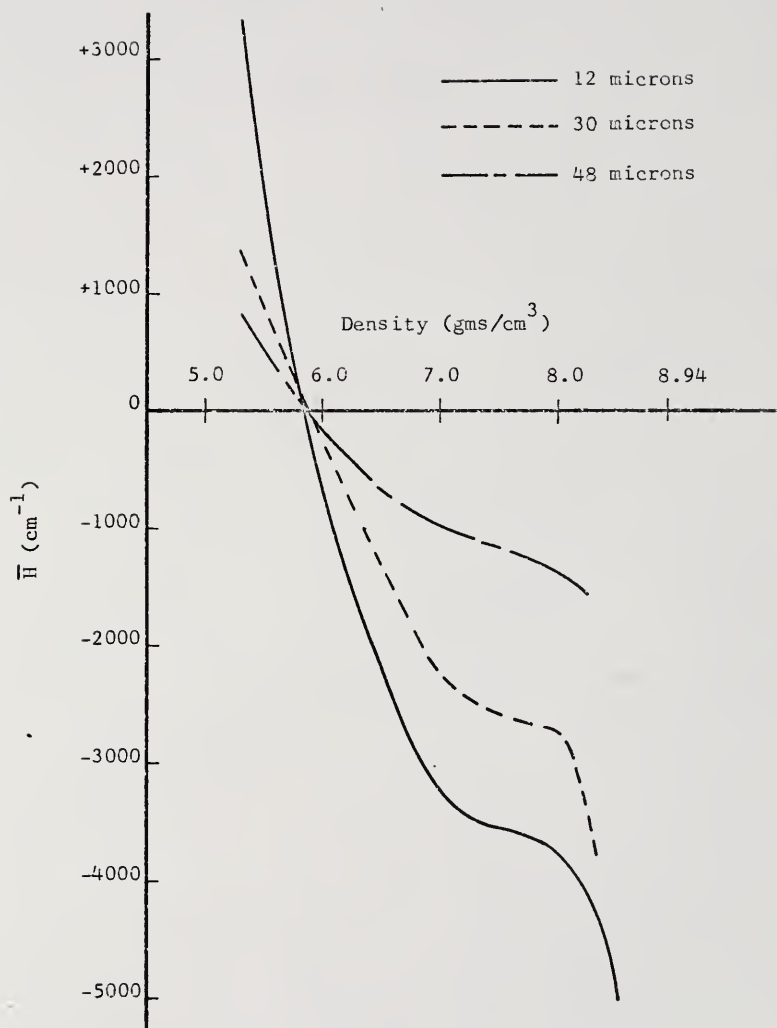


Figure 27. Comparison of the average surface curvature as a function of density for the 48, 30 and 12 micron particle sizes of spherical copper powders.

mean surface curvature of the loose stack may be estimated by

$$\bar{H} = \overline{\left(\frac{1}{r_1} + \frac{1}{r_2}\right)} \approx \frac{2}{\bar{r}} = \frac{4}{\bar{d}} \quad (15)$$

where  $\bar{d}$  is the average particle diameter for each powder size. These calculated values were used to extend the curves in Figure 27 from the experimentally determined region (approximately 6.0 to 8.3 gms/cm<sup>3</sup>) to the estimated loose stack density, 5.3 gms/cm<sup>3</sup>. The formation of permanent contacts, or weld necks, between the particles introduces negative curvature into the system and creates curvature gradients between the neck region and the positively curved surface of the nearly spherical particles. The magnitudes of these gradients control the rates of vapor and surface transport which smooth the surface and reduce the surface area in the system. The amount of negatively curved surface in the system increases with further densification and the average value of mean curvature drops rapidly through zero and becomes negative in the density range of 5.8 to 6.0 gms/cm<sup>3</sup>. Average mean curvature becomes an increasingly large negative value throughout the remainder of the first stage. The slope of the average mean curvature-density curves in the first stage, in Figure 27, is related to the change in the magnitude of the curvature gradients; as the gradients dissipate with increasing density, the slope decreases. This effect is evident also in the change in the slope produced by a change in the particle size. Curvature gradients are steeper in a fine particle size and the slope is correspondingly greater.



The end of the first stage is revealed in the average mean curvature-density relationship by an almost abrupt decrease in the slope of the curves in Figure 27. This implies that the effectiveness of the remnants of the original curvature gradients has been considerably reduced and is consistent with the attainment of a minimal surface area at the end of the first stage. The absolute minimum value of surface area possible for a given volume of porosity would exist in a system containing a single sphere. However, Rhines [1] has demonstrated that the shape changes in the first stage are localized and prevent such a structural development. This is due to the fact that the curvature gradients change the direction of material transport by vapor and surface mechanisms within distances approximating half a particle diameter. Under this limitation, the system can minimize its surface area, for a given void volume, by separating the void phase into separate spherical pores. In order to achieve this configuration the channels in the pore network must be closed. Therefore, the coincidence of a decrease in connectivity, a linear relationship between density and surface area per unit volume, and a decrease in the rate of change of surface curvature is evidence of a decrease in the ability of curvature gradients to promote shape changes in the pore network. If this were not true, then further decrease in surface area per unit volume could occur without requiring a decrease in connectivity, and the rate of change of curvature with increasing density would not be so diminished by the end of the first stage.

The evolution of average surface curvature is also sensitive to the variation in connectivity of the pore network during the second stage. As shown in Figures 17, 18 and 19, a rise in curvature occurs during the last half of the second stage. The rate of decrease in connectivity may be seen to diminish in the same range of density in Figure 26. According to DeHoff and Rhines [60], a channel can decrease in size until it attains the set of critical dimensions which render it unstable and make it collapse. The surface rounding processes of the first stage produce some channels which can close early in the second stage. The remaining channels must decrease in size through shrinkage of the solid framework. This increases the average curvature of the remaining channels and therefore of the system. The separate parts developed by the channel closure process reveal their inability to shrink by decreasing their surface area through coarsening [63] in the third stage. This process is considered to be responsible for the occurrence of a maximum value of average curvature. Thus, the evolution of average mean surface curvature, in agreement with the other geometric parameters which have been measured, strongly indicates that after an initial period (the first stage) of adjustment in the shape of the void-solid interface, the system proceeds along a path of geometric evolution consistent with the concept of a series of minimal surface area configurations. The instantaneous values of the minimal surface area are conditioned on the values of the remaining volume and connectivity of the void phase. Furthermore, and more important to this research effort, is the evidence that the average value of mean

surface curvature should be indicative of the average value of the shrinkage forces in the system. The veracity of the latter statement is substantiated in the obvious similarities in the variation with density of the average mean curvature (Figures 17, 18 and 19) and of the sintering force (Figures 7, 8 and 9). The scatter in  $\bar{H}$  data and the limited number of values do not clearly reveal the maximum in average mean curvature implied by the sintering force results. However, a maximum in average curvature has been reported by DeHoff and Slean [62] to occur at a density of 7.9 gms per cm<sup>3</sup> in an electrolytic copper powder; this is shown in Figure 28.

#### 4.3 Analysis of the Sintering Force

On the basis of the geometric arguments presented in the previous section it will be assumed in this analysis that the average surface tension forces in the system may be calculated in terms of its average value of mean surface curvature. Although it is true that the external force applied may not balance the internal forces at every location in the system, it is assumed that it does so on the average.

Using these assumptions, the average pressure,  $\bar{P}$ , acting to compress the void phase can be calculated from the basic equation

$$\bar{P} = \gamma \bar{H} \quad (16)$$

If it is further assumed that this pressure is distributed throughout the system without dilution by the solid phase, then the force component of this pressure which acts perpendicular to an area  $A$  of the sinter body is equal to  $\gamma \bar{H} A$ . The average force,  $\bar{F}$ , which counteracts the effect of the external load is given by

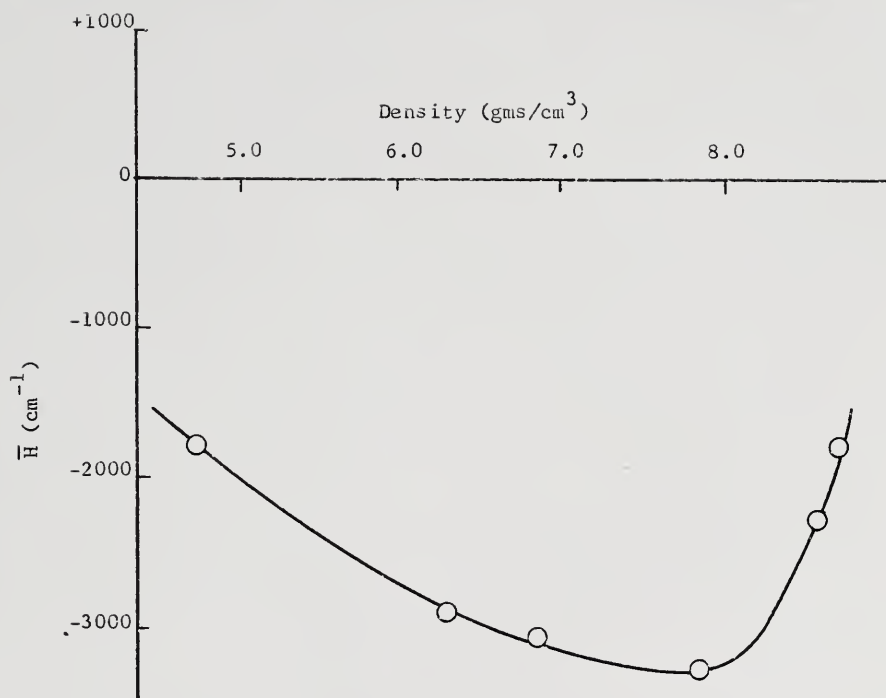


Figure 28. Variation of average surface curvature with density for a mixture of sizes of an irregular, dendritic, electrolytic copper powder [62].

$$\bar{F} = \gamma \bar{H} \bar{A} \quad (17)$$

where  $\bar{A}$  is the average cross-sectional area perpendicular to the direction of loading. This relation would be directly applicable to a system composed of porosity separated by very thin interfaces; e.g., a soap froth.

An alternative, and more realistic approach, is to consider a simple balance of forces between the external load and the sum of all force components emanating from the void-solid interface in a direction parallel to the applied load. For example, if the desired component of force per unit length is  $F_i$  and is single-valued over the length,  $l_i$ , of the line of intersection between the void-solid interface and the plane perpendicular to the applied load, then the total resolved force would be equal to the sum  $\sum_i F_i l_i$  taken over the total length of all such intersections. This sum cannot be rigorously calculated from the geometric description of the void-solid interface presently obtainable. However, the general principles of this approach may be demonstrated through the application of a simplified geometry. Consider a system containing a homogeneous spatial distribution of spherical pores of radius  $R$ . On any cross-sectional plane, the circular intersections with these pores will vary in size with the largest having a radius  $r = R$ . The force contribution from any single intersection can be calculated in terms of the curvature,  $\frac{2}{R}$ , of the system. As shown in Figure 29, the desired force component,  $F_i$ , is constant around the total length of the perimeter of the intersection. Therefore, the total force from this pore intersection, perpendicular to the cross-sectional

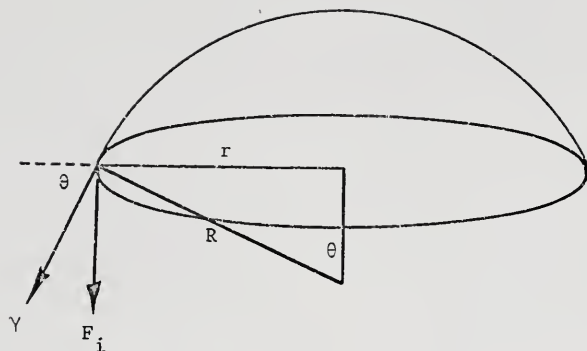


Figure 29. Resolution of surface tension forces emanating from the cut surface of a spherical pore in a direction perpendicular to the sectioning plane.

plane, is  $2\pi r F_i$ . Since  $\sin \theta = \frac{F_i}{\gamma} = \frac{r}{R}$ , this becomes  $\gamma \left(\frac{2}{R}\right) \pi r^2$  or  $\gamma H A$ , where  $A$  is the area of the circular intersection. The total force in the system acting across the intersecting plane is equal to the sum

$$F = \gamma H \sum_j A_j \quad (18)$$

where  $A_j$  is the area of the  $j^{\text{th}}$  circular intersection. The total area of pore intersections on a cross-sectional plane of area  $A$  is equal to  $A_{AV} A$  where  $A_{AV}$  is the area fraction (equivalent to the volume fraction) of porosity in the system. Therefore, the working form of this relation becomes

$$\bar{F} = \gamma \bar{H} \bar{A}_{AV} \bar{A} \quad (19)$$

The effect of increase in curvature and decrease in area fraction of porosity (i.e., increase in density) on the sintering force predicted

by this relation may be shown as follows. The maximum component of the surface tension occurs when the radius of the circular intersection in Figure 29 is equal to the radius of the sphere; i.e., when the intersecting plane cuts the diameter of the sphere. Under these conditions  $\theta$  is  $90^\circ$  and the force component is equal to the surface tension,  $\gamma$ . Allowing the sphere to shrink is equivalent to increasing the density of the system. However, this decreases the total line length (perimeter of the circle) over which the force,  $\gamma$ , exists and therefore predicts a decrease in the sintering force with increasing density. This is contrary to the experimental results which show an increase in the sintering force over the entire second stage of sintering. This reveals the inadequacy of the sphere model in representing the geometrical evolution of the multiply-connected pore network in real systems. However, the principle of a balance of forces expressed by the relation derived rigorously for the spherical model is correct. Examination of equation (19) will show that if the increase in curvature,  $\bar{H}$ , is greater than the decrease in the area fraction of porosity,  $\bar{A}_{AV}$ , then an increase in the sintering force,  $\bar{F}$ , is predicted. This is not possible in a system of spheres since their curvature, intersected area and volume relationships are fixed by their shape. However, in real sintering systems, the shape of the pore network is constantly changing and  $\bar{H}$  and  $\bar{A}_{AV}$  can vary somewhat independently. The change in curvature for a system of shrinking spheres would be smooth and continuous, but the change in average mean surface curvature for a real sintering system is sensitive to the changes in connectivity of the void network, as is evident by a comparison of Figure 26 and Figure 27. Therefore, equation (19) should be

applicable to real sintering systems for which the average mean surface curvature,  $\bar{H}$ , and the average area fraction of porosity,  $\bar{A}_{AV}$  on an average cross-sectional area,  $\bar{A}$ , are known.

#### 4.31 Comparison of predicted and experimentally measured sintering forces

The sintering forces predicted by equations (17) and (19) are presented as a function of density in Figures 30, 31 and 32, for comparison with experimentally obtained values. The value of surface tension,  $\gamma$ , used for the calculations was 1650 dynes per cm (1.68 gms per cm), the accepted value for copper at 1000°C. The temperature coefficient of the surface tension for copper as reported by Udin et al. [12] is approximately 0.50 dynes per cm per °C. A variation in temperature of 100°C, corresponding to the range of temperatures (950 to 1050°C) investigated in this research, produces a total change in  $\gamma$  of only 50 dynes per cm, or approximately 3 per cent. Thus, the effect of temperature is well within the normal scatter of the experimental values of the sintering force and was not included in the calculation of the predicted values.

The force values predicted by equation (17) are designated as maximum values since they correspond to equation (19) when the area (volume) fraction of porosity is unity; i.e., when the volume of the solid phase is essentially negligible. Although the predictions of equation (17) are, as expected, greater than the experimental values, the qualitative behavior of the two curves as a function of density is strikingly similar. Although qualitative in nature, this observation



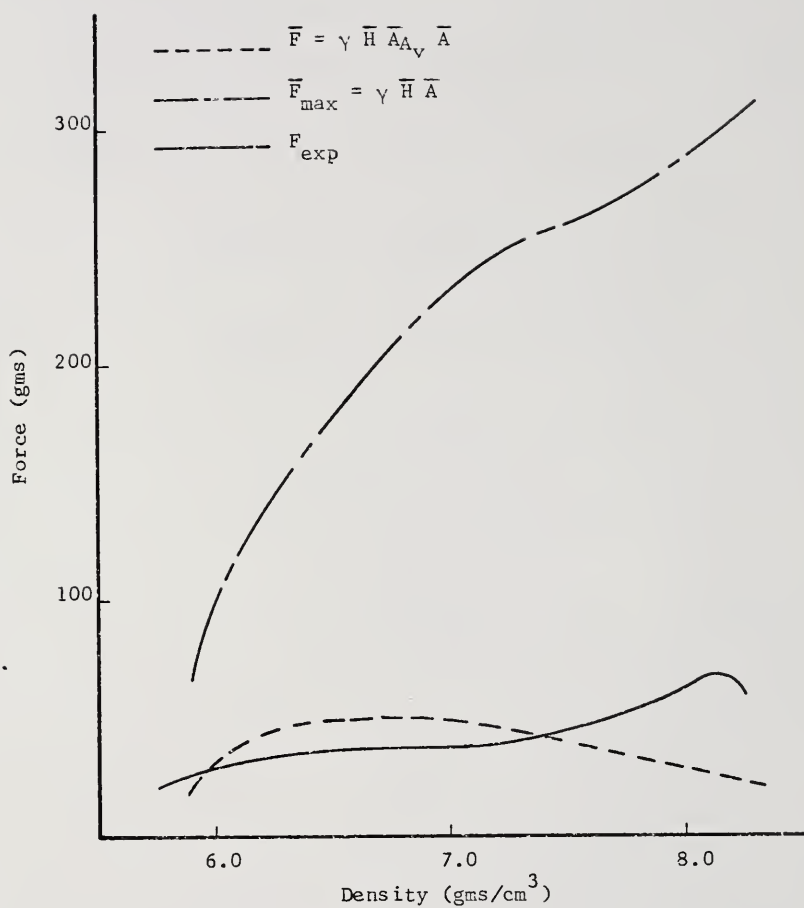


Figure 30. Comparison of the experimental values of the sintering force with predicted values for the 48 micron particle size powder.

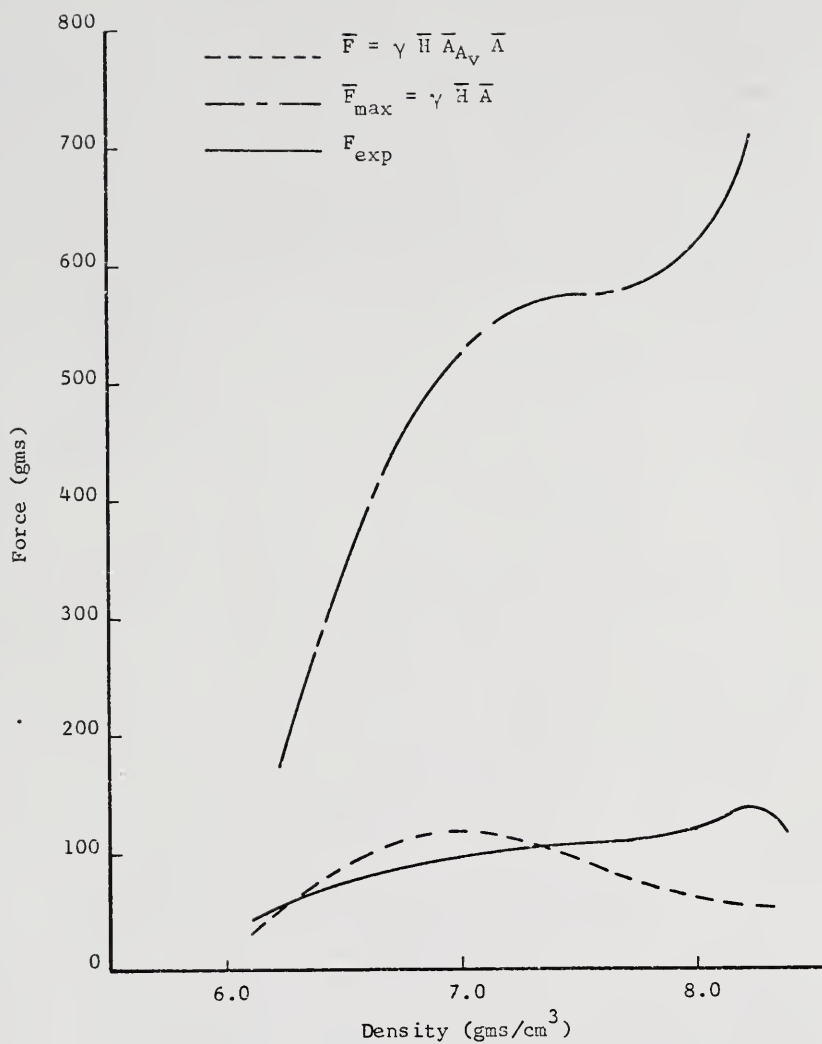


Figure 31. Comparison of the experimental values of the sintering force with predicted values for the 30 micron particle size powder.

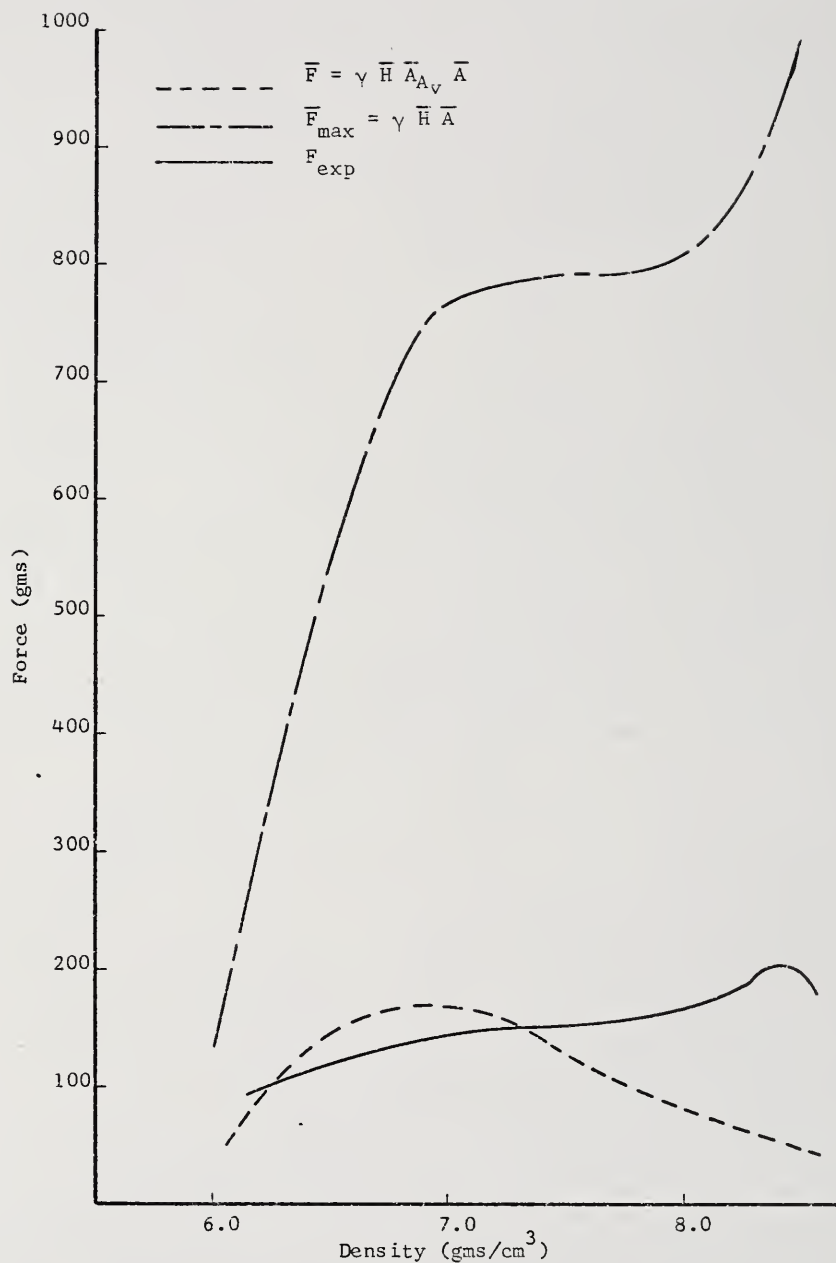


Figure 32. Comparison of the experimental values of the sintering force with predicted values for the 12 micron particle size powder.

definitely relates the sintering force, as defined in this research, to the average value of the mean surface curvature of the sintered structure, and strengthens the assumptions made in regard to this relation.

The forces predicted by equation (19) are in better agreement with the experimental values; however, the two curves do not possess the same shape. Although the predicted curve rises rapidly from zero at zero average curvature to the proper level of the sintering force, it begins to decrease early in the second stage of densification. This discrepancy can be qualitatively reconciled in the following way. In the experimental measurement of the sintering force the external force is applied to balance the shrinkage of the system. Therefore, elements of the void phase which contribute the most to the overall shrinkage are primarily responsible for the level of external load required to balance the shrinkage. The values of average surface curvature and area fraction should be more heavily weighted in favor of these elements of the void phase. The recognition of these elements on a two-dimensional microsection cannot be unambiguously performed. It may be assumed that the smaller pores on a two-dimensional section are those which will continue to shrink, or if they are intersections with channels, to collapse, but a quantitative delineation on this basis must be considered arbitrary. It is obvious that division of the void volume into portions based on their relative contribution to shrinkage will reduce the selected area of porosity below the average value,  $\overline{A_{AV}}$ . However, the portions which do produce volume changes in

the system will possess the higher values of curvature in the system since they decrease in size. The elements of the void phase which do not shrink will decrease their surface area (and therefore their energy) through conglomeration; this process reduces their curvature. The primary mechanism of densification (shrinkage) in the second stage is channel closure. Therefore, the ability of any portion of the void phase to experience further channel closure may be a reasonable criterion for estimating its contribution to shrinkage of the system. Thus, the fraction of the void volume which would not be expected to contribute to the shrinkage forces would increase with the increase in number of parts of the void phase separated from the rest of the pore network by channel closure. Some justification for this argument exists in the shape of the curves predicted by equation (19) in Figures 30, 21 and 32. For each particle size the predicted values begin to decrease prematurely in the range of density where the number of separate parts of the void phase begins to become significant, as shown in Figure 26. The inclusion of the non-shrinking, low curvature elements reduces the experimentally measured values of average curvature and in this way reduces the sintering forces predicted by equation (19). Thus, it is suggested that with increased knowledge of the details of the geometry of the system, equation (19) would accurately predict the average forces which promote shrinkage in the system beyond the first stage of sintering.

#### 4.4 Comparison of the Results of This Research with Previous Investigations

Other than the present research there are only two known experimental analyses of the effect of uniaxial tensile forces on the shrinkage behavior of powdered solids during sintering. One was the first attempt to measure the sintering force in copper by Young [46]. The other was an attempt by Dawihl and Rix [64] to discern the effect of tensional constraint on the sintering behavior of powder compacts of cobalt.

Young measured the force of sintering in a -325 mesh (-44 microns) irregular copper powder by suspending various weights from a series of identically prepared specimens. He found that the sintering force increased from 21 to 35 gms with an increase in density from 3.98 to 5.37 gms per  $\text{cm}^3$  in specimens with an initial cross-sectional area of approximately  $.240 \text{ cm}^2$ . An analysis of Young's results cannot be made since the geometric description necessary is not available. However, the magnitude and variation with density of his measured sintering forces agree well with the results obtained in this research.

Dawihl and Rix utilized a pulley to attach weights to sintering cobalt powder compacts placed horizontally in the sintering furnace. Using various weights they measured the effect of increasing stress (calculated on the basis of an original cross-sectional area of  $.1963 \text{ cm}^2$ ) on the relative amounts of longitudinal and radial shrinkage of cylindrical specimens. The range of applied stresses was sufficient to encompass the stress which resulted in zero shrinkage in the direction of the applied load. From this stress value and the original

cross-sectional area the sintering force could have been calculated had these investigators had the present concept of the sintering force. Although the compacts were sintered for a constant length of time, the use of three sintering temperatures (1000, 1200 and 1350°C) resulted in a limited range of densities and allows an estimate of the variation of the sintering force with density. The results indicate a decrease in sintering force from 650 to 530 gms over the range of 88 to 94 per cent of the theoretical density of cobalt. This is in agreement with the results of this research which document a decrease in sintering force in copper in the range of 90 to 95 per cent of theoretical density. The magnitudes of the sintering forces estimated from the data of Dawihl and Rix are considerably higher than the values found for copper but are reasonable for the powder particle size which they reported to be approximately 1 micron. There is no known value of the surface tension of cobalt with which to substantiate this conclusion.

#### 4.5 Application of the Sintering Force to the Measurement of Surface Tension of Solids

The sintering forces predicted by equation (19) agree very well with experimental values in the range of density corresponding to the end of the first stage and the beginning of the second stage of sintering. At the maximum deviation in this range, the adjusted values of surface tension required to produce complete agreement are 1315, 1320 and 1400 dynes per cm for the 48, 30 and 12 micron particle sizes, respectively. These values are lower than the expected value

of 1650 dynes per cm by 21.5, 20 and 15 per cent. The increase in agreement with decrease in particle size is considered to be the result of increased accuracy in the measurement of the sintering force made possible by the higher rates of shrinkage of the finer powder. Thus, experimental determination of the sintering force, average surface curvature and the density of a suitably prepared sinter body will allow a reasonable estimate of the surface tension of the powdered solid. The difficulties in experimental determination of the proper values of  $\bar{H}$  and  $\bar{A}_{AV}$  to use in equation (19), discussed previously, restrict this application of the sintering force concept to a narrow range of density. However, it has been demonstrated [38] that delineation of the first and second stages of sintering can be accomplished in a wide range of sinterable materials through experimental determination of the surface area per unit volume-density relationship.

Objections have been made to the use of metal foils [12] and of wires [65] based on their tendency to break up into globules during the test. While it is true that the void-solid interface experiences changes in shape during densification, the concept of minimal surface area for any given value of connectivity and void volume implies the existence of a quasi-equilibrium state corresponding to each minimum surface area configuration. Quantitative description of the quasi-equilibrium state corresponding to the density for which the sintering force measurement was made is possible through quantitative metallography. The procedure used for experimental determination of the sintering force allows a decision as to the



force required to balance shrinkage within the same time interval required for a measurable change in the curvature of the void-solid interface. Thus, the use of a sinter body to measure surface tension offers two distinct advantages. First, the measurement corresponds to a free solid surface in a condition of quasi-equilibrium. Second, this method can extend the measurement of surface tension to the wide range of materials which are sinterable but cannot be reasonably formed into wires or foils.

#### 4.6 Kinetics of the Sintering Process

The results obtained in this research have established that the surface tension forces which promote densification of the system may be characterized by the experimentally defined sintering force which is single-valued for any given state of the system. In order to determine quantitatively the relation between microstructure and sintering kinetics, it is necessary to analyze the manner in which the complex structure that exists in a sinter body responds to these forces.

##### 4.61 Estimation of stresses created by external load

The effect of internal defects, such as porosity, on the mechanical behavior of solids can be very pronounced and has been the subject of extensive theoretical and experimental analyses. The reduction in strength resulting from porosity is generally attributed to the constraints to plastic flow arising from the presence of notches in the system. However, it has been observed (e.g., in sintered iron compacts [66]) that the tensile strength of sinter bodies can be

independent of original powder particle size or shape and a function only of the density of the system. Such an observation is not easily reconciled through the consideration of notch type stress concentrations alone.

The yield strength of the spherical copper powder used in this research has been determined by Gillard [67] and is presented in Figure 33. There was no effect of particle size over the wide range (approximately an order of magnitude) of particle sizes investigated. The strength decreases with decreasing density at a rate faster than would be expected on the basis of decrease in area fraction of solid, indicating that the operating stresses are significantly higher than those calculable from the average solid area on a cross-sectional plane. In addition to the effect of stress concentrations, the strength can also be reduced by distribution of the applied load over a cross-sectional surface which intersects minimum amount of solid phase. This surface would necessarily be non-planar, as opposed to the plane surface which would intersect an average amount of solid phase; i.e.,  $\bar{A}_{A_S} \bar{A}$  where  $\bar{A}_{A_S}$  is the average area fraction of solid. The strength of a sintered specimen relative to the fully dense solid can be used to estimate the effective supporting area in the sinter body in the following way. The yield stresses in Figure 33 are calculated in terms of the original external dimensions of the specimen. The ratio of the force which produces yielding in a partially dense sinter body to the corresponding force in a fully dense specimen with the same apparent cross-sectional area is given by

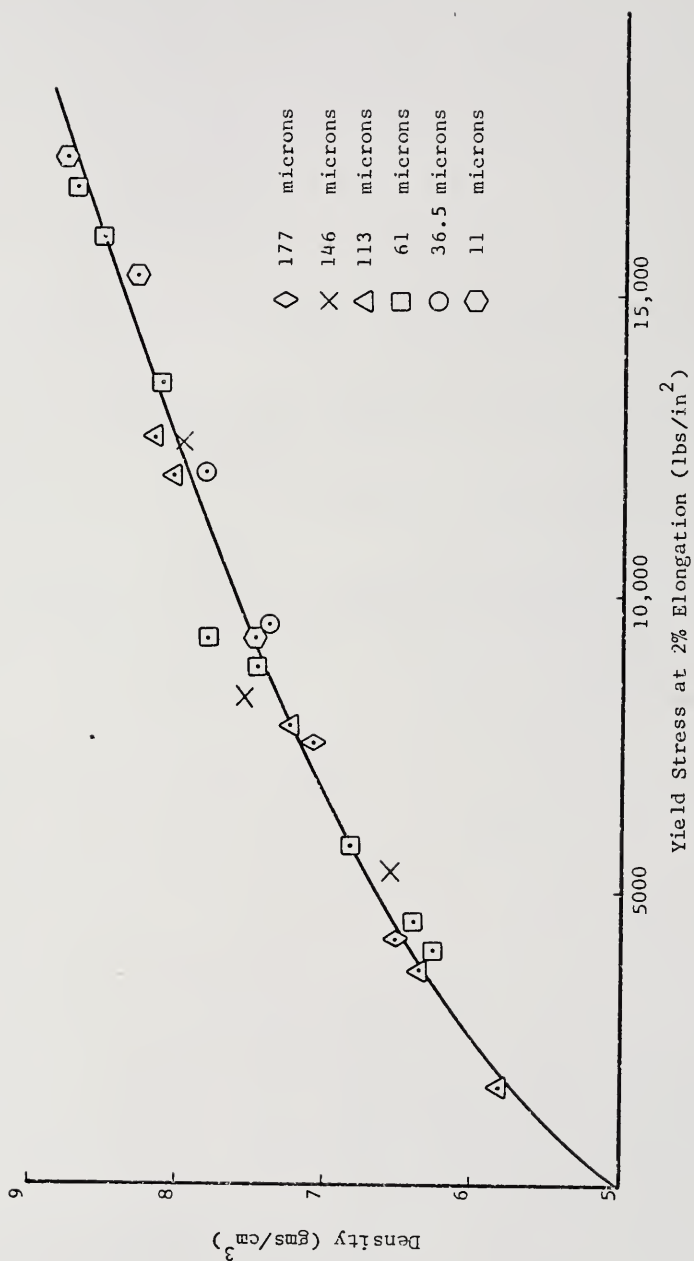


Figure 33. Room temperature yield stress at 2 per cent elongation as a function of density for a range of particle sizes of the spherical copper powders used in this investigation [67].

$$\frac{F_{\rho y}}{F_{s y}} = \frac{F_{\rho y}/A}{F_{s y}/A} = \frac{\sigma_{\rho y}}{\sigma_{s y}} \quad (20)$$

where  $\rho$  and  $s$  refer to the sinter body of density  $\rho$ , and the fully dense specimen and  $y$  indicates the yield point. If it is assumed that the difference in observed strengths for the two specimens is only a result of difference in effective supporting solid area, then

$$\frac{\sigma_{\rho \text{eff}}}{\sigma_{s \text{eff}}} = \frac{F_{\rho y}/A_{\rho \text{eff}}}{F_{s y}/A_{s \text{eff}}} = \left( \frac{\sigma_{\rho y}}{\sigma_{s y}} \right) \left( \frac{A_{s \text{eff}}}{A_{\rho \text{eff}}} \right) = 1$$

and

$$A_{\rho \text{eff}} = \left( \frac{\sigma_{\rho y}}{\sigma_{s y}} \right) A_{s \text{eff}} \quad (21)$$

The operation of stress concentrations in the sintered specimen prevents the effective area,  $A_{\rho \text{eff}}$ , from being a purely physical area. However, this does not preclude the use of this mathematically defined area to estimate the effective operating stress in a sinter body under any applied load. For a fully dense specimen,  $A_{s \text{eff}}$ , is equal to its cross-sectional area; therefore, for calculation of  $A_{\rho \text{eff}}$  for the sintering force specimens  $A_{s \text{eff}}$  corresponds to a solid specimen of the same cross-sectional area as the sintered specimen. The values of  $A_{\rho \text{eff}}$  calculated from equation (21) are presented in Figure 34. The supporting solid area on an average plane,  $\bar{A}_{As} \bar{A}$ , is presented for comparison; as expected, the effective supporting areas are considerably lower.

The stresses in the specimen resulting from the external force required to stop shrinkage of the system may be calculated from the relation

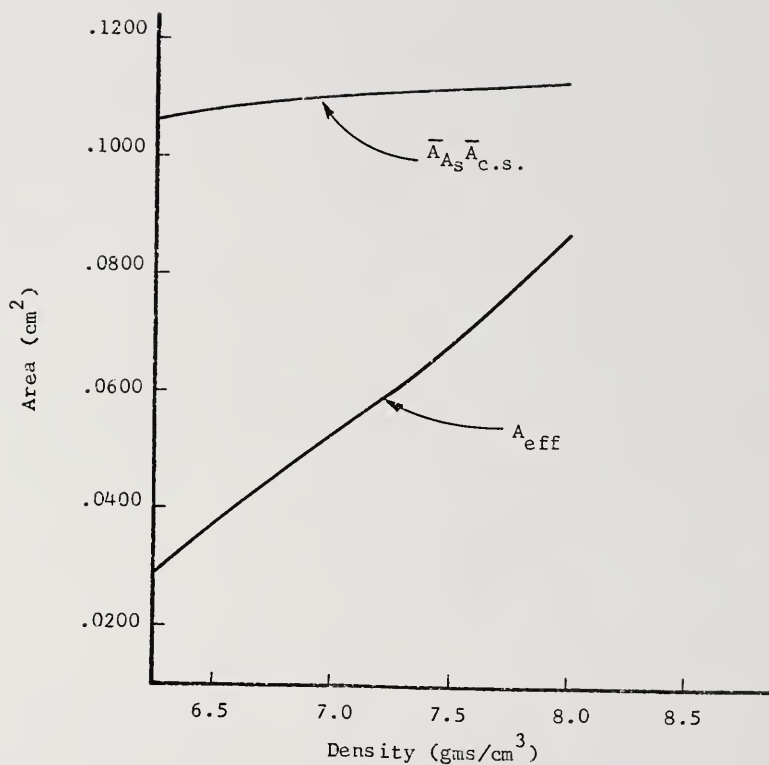


Figure 34. Variation of the average solid area and the effective solid area estimated from experimentally observed mechanical behavior with density for spherical copper powders.

$$\sigma = \frac{F}{A_{p_{eff}}} = \left( \frac{F}{A} \right) \left( \frac{\sigma_{s_y}}{\sigma_{p_y}} \right) \quad (22)$$

where  $F$  is the experimentally measured sintering force,  $A$  is the apparent cross-sectional area, and  $\sigma_{s_y}$  and  $\sigma_{p_y}$  are the yield strengths for solid copper and a sintered specimen of density  $\rho$ , respectively. The stresses calculated from equation (22) are presented in Figure 35 for the 48, 30 and 12 micron particle sizes.

#### 4.62 Correlation of the sintering force with shrinkage rates

It has been demonstrated that through empirical treatment of the experimentally documented mechanical behavior of the sintered structure, reasonable estimates of the effective operating stresses created by the external force required to stop shrinkage of the system can be obtained. At the moment of balance, the deformation rate which should result from these stresses may be considered to be equivalent in magnitude to the linear shrinkage rate which would exist in the system in the absence of external constraint. The relation between the operating stresses and the shrinkage rate can be shown to be consistent with the commonly observed high-temperature deformation characteristics of copper.

Isothermal deformation rate laws for high temperature creep have the general form

$$\dot{\epsilon} = k \sigma^n \quad (23)$$

where  $\dot{\epsilon}$  is the linear strain rate produced by the stress,  $\sigma$ .

The exponent of stress,  $n$ , is found to vary with the stress level

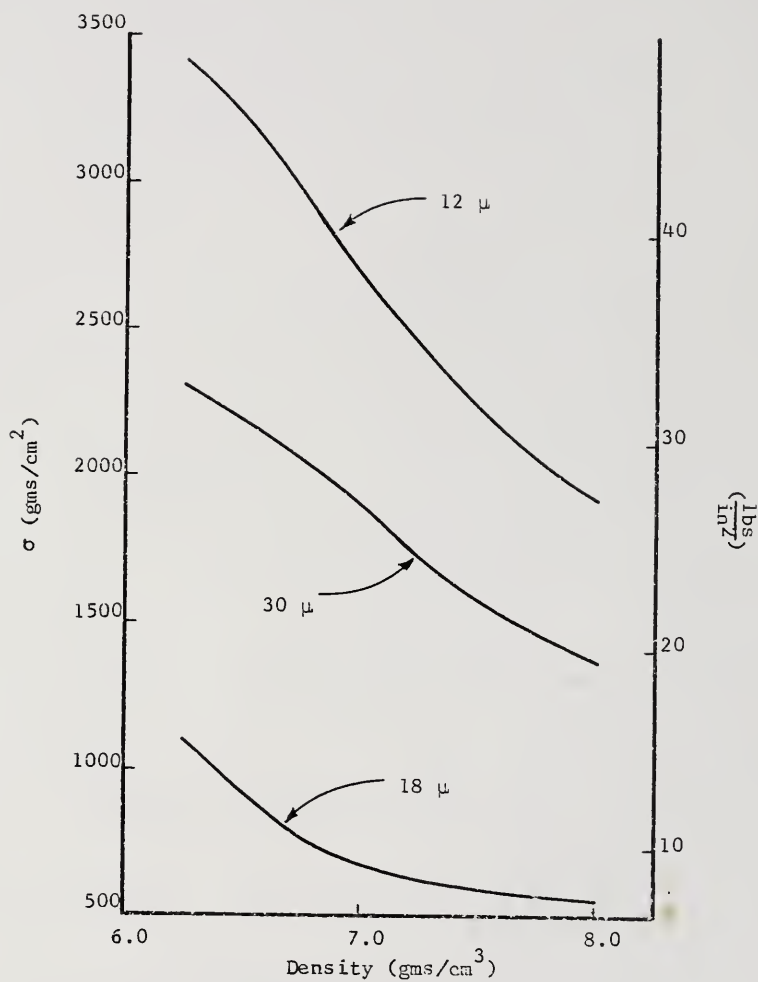


Figure 35. Estimated operating stresses created by externally applied force on sintering force specimens.

as shown in Figure 36; for pure metals at low stresses  $n = 1$ , at high stresses  $n = 4.5$ . The effect of the scale of the microstructure (grain size) is significantly greater in the low stress region. Udin et al. [12] reported  $n = 1$  for creep of the pure copper wires used to determine the value of surface tension of copper. They applied stresses up to 850 gms per cm<sup>2</sup> (12 lbs per in<sup>2</sup>). In the measurement of surface tension in copper foils, Pranatis and Pound [68] applied stresses ranging from 10 gms per cm<sup>2</sup> (.15 lbs per in<sup>2</sup>) to 2600 gms per cm<sup>2</sup> (36 lbs per in<sup>2</sup>) and found  $n = 1$ . For much higher stresses, approximately 28,000 gms per cm<sup>2</sup> (400 lbs per in<sup>2</sup>), Barrett and Sherby [69] reported  $n = 4.8$  for pure copper.

The linear shrinkage rates of the 48 and 30 micron particle sizes used in this investigation have been determined at 1000°C by Lemons [70] and Eilbeck [71], respectively. They are presented as a function of density in Figure 37. Substitution of these rates and the effective stresses at the same density into equation (23) yields the plots in Figure 38. The values of  $n$  obtained are 4.0 and 5.6 for the 48 and 30 micron sizes, respectively. However, the level of stresses estimated for these systems (Figure 35) is equivalent to or below the level of stresses for which it is expected that  $n = 1$  for pure copper. Therefore, an effect of the scale of the microstructure must be included. The range of density over which the stress and shrinkage rate data extend encompasses a significant evolution of the sintered structure; both the grain boundary array and pore network coarsen with increasing density. Since the fine microstructure



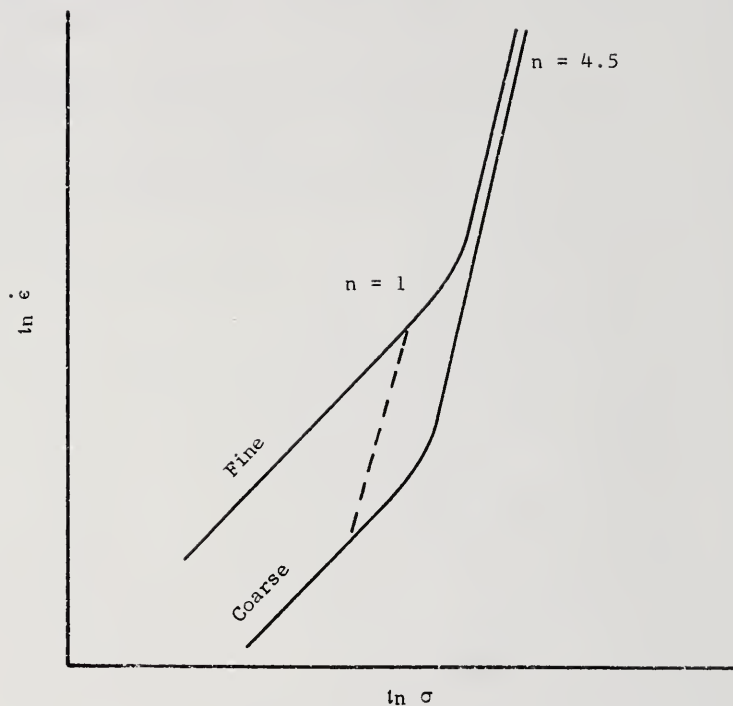


Figure 36. The relation between strain rate,  $\dot{\epsilon}$ , and stress,  $\sigma$ , as affected by the scale of the microstructure for isothermal high temperature deformation of pure metals.

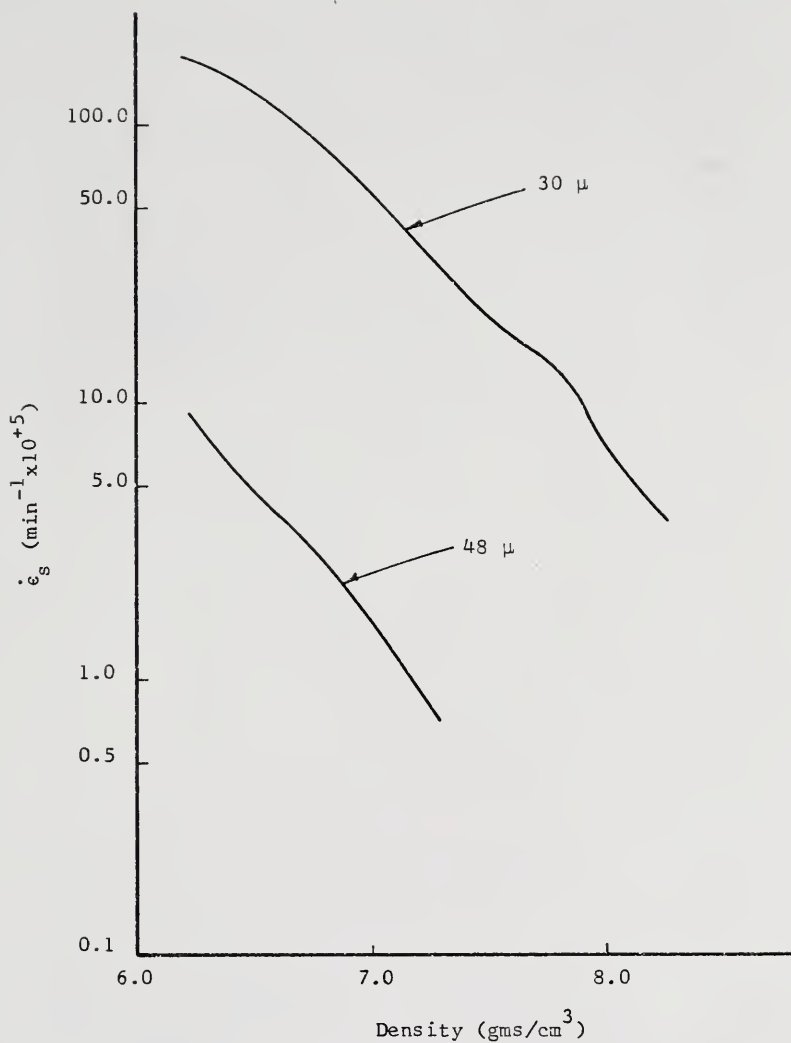


Figure 37. Variation of experimentally determined linear shrinkage rates with density for the 48 [70] and 30 [71] micron particle sizes of spherical copper powder.

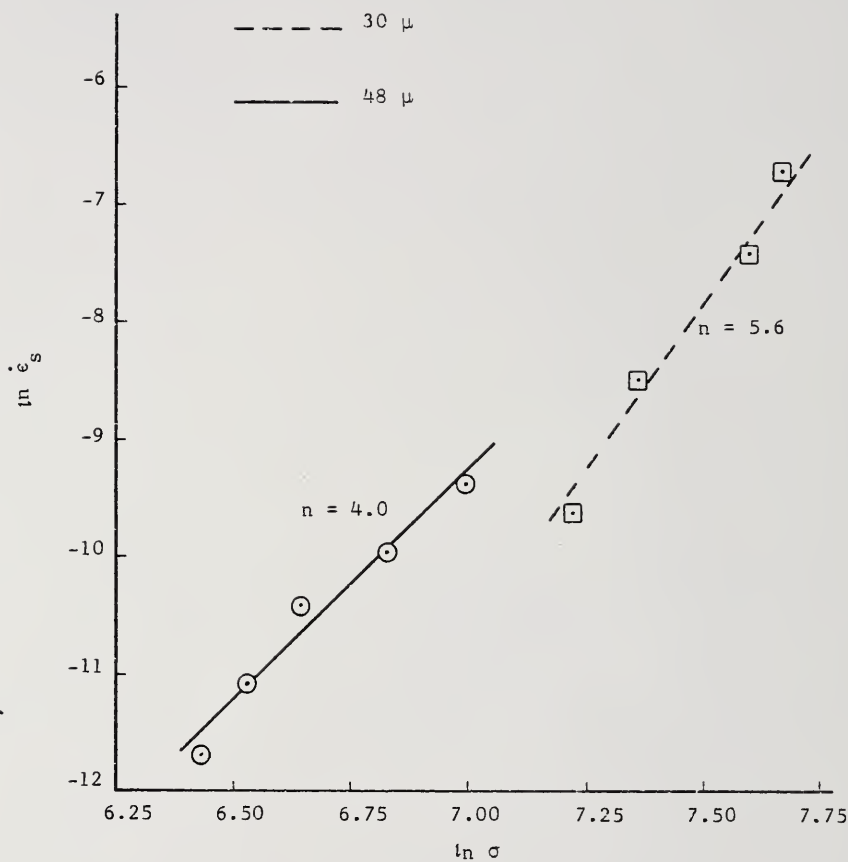


Figure 38. Relationship between linear shrinkage rates and estimated effective stresses for the 48 and 30 micron particle sizes of spherical copper powder.

corresponds to high stresses and the coarse microstructure to low stresses, the effect of structural evolution can be expected to be similar to the dashed line in Figure 36 and is consistent with the high values of  $n$  obtained from the plots in Figure 38.

The effect of grain size on the strain rate for a given stress in the region where stress and strain rate are linearly related ( $n = 1$ ) has been found to be consistent with the relation

$$\dot{\epsilon} \propto \frac{\sigma}{\bar{D}^2} \quad (24)$$

where  $\bar{D}$  is the average grain size. This relation has been theoretically derived by Herring [11] based on a stress-directed volume diffusion mechanism which utilizes grain boundaries as sinks and sources of vacancies. The geometric parameter which is sensitive to the scale of the microstructure of a sinter body is the mean lineal intercept,  $\bar{\lambda}_s$ , in the solid phase. This can be calculated from the relation [61]

$$\bar{\lambda}_s = 4 \frac{V_{Vs}}{S_v} \quad (25)$$

where  $V_{Vs}$  is the average volume fraction of solid phase and  $S_v$  is the surface area per unit volume in the system. Substitution of the value of  $\bar{\lambda}_s$ , together with the values of stress and shrinkage rate for the corresponding density, into relation (24) produced the data plotted in Figure 39. The resulting slopes of 1.16 and 0.98 for the 48 and 30 micron particle sizes are considered to be in excellent agreement with the expected value of unity.

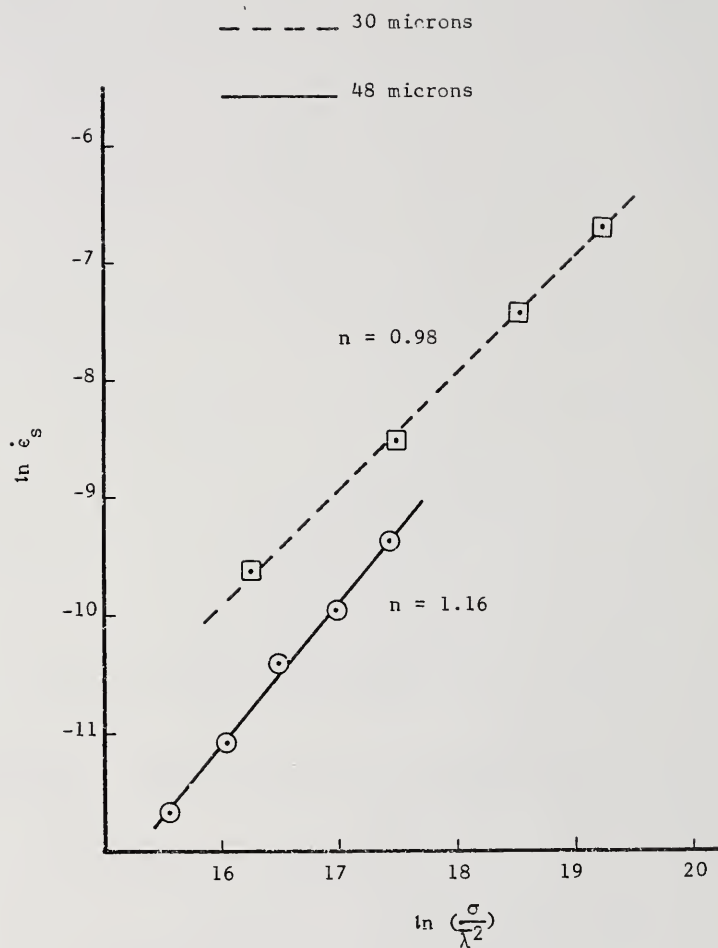


Figure 39. Correlation of linear shrinkage rate--estimated operating stress relationship with deformation rate law based on stress-directed diffusion.

#### 4.63 Comments on the mechanism of shrinkage

Within the field of sintering research there currently exist two schools of thought with respect to the mechanism of shrinkage; one supporting volume diffusion [19,31] and the other, creep processes [1,17]. Both mechanisms are considered to originate in the effect of surface tension on the structure. It was not the purpose of this research to develop arguments in support of either viewpoint but rather to establish general and fundamental relationships drawn from the sintering behavior of complex, three-dimensional sintered structures which could serve as a framework to which mechanistic arguments must conform in order to explain the behavior of real systems; not just the simple models from which they are typically derived. However, the results of this effort warrant a few, brief comments on the mechanism of shrinkage.

The analysis of the last section clearly established a relation between the microstructure and kinetics of shrinkage of a sintering system through application of the concept of the sintering force. The response of the structure to the sintering force was found to be consistent with a rate law based on deformation by stress-directed diffusional processes. It must be noted that the experimental verification of this mechanism for creep of pure metals is limited. However, experimental creep data for copper [12,68], gold [72], nickel [73] and  $\delta$ -iron [74] agree well with values predicted by the Herring [11] creep analysis. The results of the present investigation have extended these observations to the response (creep) of porous copper bodies

to an external load and further, to the shrinkage of these systems through the relation of the sintering force to the surface tension forces promoting shrinkage. This dual observation implies a similarity between the creep of solids under low stresses and the shrinkage of sintering systems. Finally, it is highly significant that in all observations of creep of metals conforming to the Herring [11] analysis (relation (24)), the magnitude of the applied stresses was equivalent to the stresses resulting from surface tension forces in the system.

## CHAPTER V

### CONCLUSIONS

1. The sintering force, defined as the external force required to stop contraction of a sinter body in the direction of the applied force, is an experimentally measurable and reproducible property of the sintered structure.

2. The sensitivity of the sintering force to the surface tension forces promoting shrinkage is established by the qualitatively identical variation with density of the sintering force and the average value of mean curvature of the void-solid interface.

3. A quantitative relationship exists between the sintering force and the average value of the capillary forces in a sintering system which can be approximated by the equation  $F = \gamma \bar{H} A_{AV} A$ , where  $F$  is the sintering force,  $\gamma$  is the surface tension of the solid,  $\bar{H}$  is the average mean curvature,  $A_{AV}$  is the area fraction of void phase and  $A$  is the cross-sectional area of the specimen.

4. The topological changes of the void-solid interface within a sintering system are directly related to the system's sintering behavior through their effect on the evolution of mean surface curvature.



5. The rate of shrinkage of copper powder systems, produced by the capillary forces within them, is mathematically consistent with the high temperature creep behavior of solid copper under low stresses; an implication that the two processes occur by similar mechanisms.

## APPENDICES

## APPENDIX I

### APPLICATION OF THE PRINCIPLES OF TOPOLOGICAL GEOMETRY TO THE DESCRIPTION OF THE SINTERING PROCESS (after F. N. Rhines [1])

Throughout the preceding text, it has been pointed out that the use of the principles of topology provides more insight into the complexities of sintered structures than is possible through the use of Euclidean geometry alone. The pertinent features and utility of this approach were first demonstrated by Rhines [1]. A synopsis of his original development follows.

Topological geometry [75] is concerned with closed surfaces and is insensitive to the dimensionality or inclosed volume of such surfaces. The topological nature of closed surfaces is not changed by their deformation as long as they are not cut or joined. This is demonstrated by Figure 40(a). Surfaces are topologically described by the magnitude of their genus. Surfaces which possess obvious differences in dimension and Euclidean shape can be topologically equivalent. Each of the various surface shapes in Figure 40(a) which have the same genus can be formed by deformation of another. The magnitude of the genus of a surface is revealed by counting the number of cuts which can be made before separating the surface into two separate parts. For surfaces of genus zero, no cuts can be made. For surfaces of genus 1 no more than one cut can be made. In similar fashion the

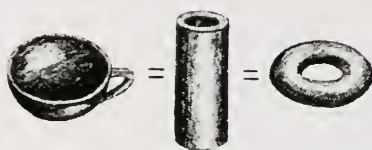
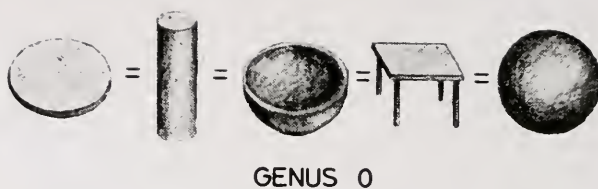
genus of more complex surfaces can be determined. For example, the genus of the surface enclosing the solid framework formed by sintering solid particles can be determined by counting the number of interparticle connections which have to be cut to reduce the genus to zero.

The ability of this topological parameter, genus, to reveal subtle changes in a particle stack is shown in Figure 40(b). The attachment of a fifth particle through a single contact to a four-particle stack with an original genus of 3 does not change the genus. However, attachment at a two- or three-point contact position increases the genus to 4 and 5, respectively. This demonstrates that the genus,  $G$ , of a mass of interconnected particles is equal to the difference between the number of interparticle contacts,  $C$ , and the number of particles,  $P$ , plus one to start the process; i.e.,

$$G = C - P + 1 \quad (26)$$

Thus, as long as the particles have no internal surfaces, the genus of the surface enclosing a particle framework can be evaluated by counting the number of particles and the number of their interconnections.

The evolution of the void-solid interface during the progression of the system from a loose particle stack toward complete densification, can be separated into stages on the basis of changes in its genus. This is demonstrated in Figure 41(a). Interparticle contacts can grow without affecting the magnitude of the genus. However, when they impinge they will close the openings among adjoining particles and decrease the genus of the system. The closure of all of these



GENUS 2



Figure 40(a). Examples of bodies bounded by surface of genus zero, one and two.

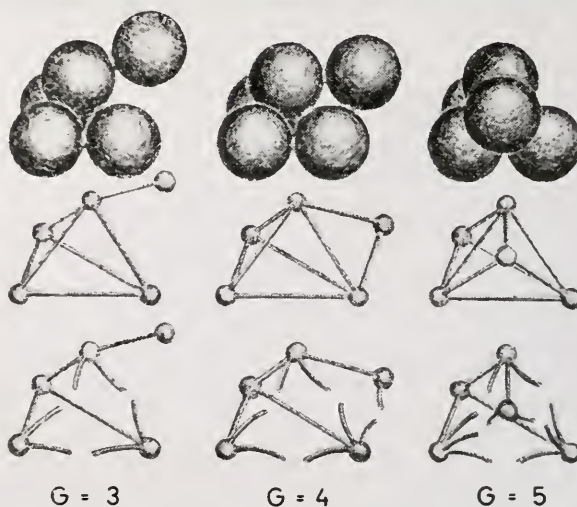


Figure 40(b). Variation of genus with number of contacts per particle.

openings in the system will produce many separate, or isolated, parts of the void phase each with a surface of genus zero. Therefore, the genus of all surface is zero and remains so as the number of separate parts of the surface (isolated pores) decrease in number throughout the remainder of the sintering process. Thus, in the first stage the genus is constant at  $C-P+1$  during the growth of weld necks, in the second stage it decreases from  $C-P+1$  toward zero, and in the third stage genus is constant as the isolated pores decrease in number.

All spontaneous geometric changes in a sintering system must occur through a decrease in surface energy, and therefore surface area. Densification can occur only by a decrease in the average distance between particle centers in the system. Decreasing the volume of the system by this process does not require any change in the genus or number of separate parts of the void-solid interface. Although it is true that both the genus and number of pores must go to zero before full densification can be attained, the pore volume remaining in the system when this occurs can be arbitrarily small.

The decrease in surface area through smoothing and rounding of the void-solid interface can also proceed independently. As shown by the bottom example in Figure 41(b), a pore surface which has become isolated by closure of the interconnections, or channels, in the pore network can reduce its surface area by spheroidization at constant volume; i.e., without densification. Surface decrease ceases when the surface has attained the shape of a sphere, the minimal surface area configuration for a surface of genus zero. A minimal surface area

# STAGES OF SINTERING

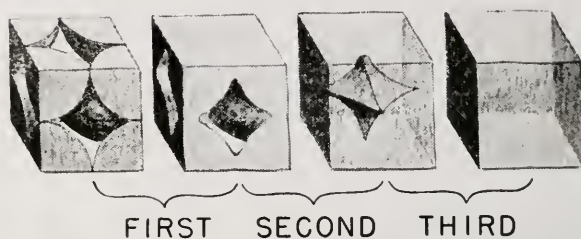


Figure 41(a). Separation of sintering into three stages on the basis of changes in genus of the void-solid interface.

## ROUNDING

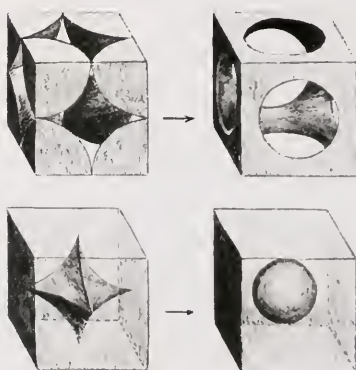


Figure 41(b). Effect of genus of the void-solid interface on its minimal surface area configuration.

configuration can also be reached for surfaces with non-zero genus. As shown in the top example in Figure 41(b), a considerable decrease in surface area can be produced by surface rounding without densification or change in the number or genus of the pore surfaces. The amount of surface area remaining after this process will be a minimum for the existing values of the void volume and genus of the void-solid interface. However, for surfaces with genus greater than zero, the value of the minimal surface area is greater than for surfaces with genus zero. Therefore, once a minimal surface area is attained, further decrease in the genus of the surface through closure of the channels of the pore network presents a new goal of minimal surface area toward which the system can proceed. If the channels, which link together the void spaces in unit cells similar to the top example in Figure 41(b), are considered to be cylindrical in shape, then the criterion for their closure may be argued. Soap film experiments [76] have revealed that films of cylindrical shape will collapse in the middle and form two parts when their ratio of length to circle diameter is greater than  $\pi$ . If this is assumed to be analogous to channel closure in a pore network, then individual channels will close upon the attainment of some set of critical dimensions. Shrinkage of the solid framework at constant genus will increase the length to diameter ratio of the existing channels in the pore network toward the value required for closure. If the minimal surface area configuration is attained for each set of values of density and genus, then these variables will be interrelated during the evolution of the system toward genus zero.



## APPENDIX II

### THE QUANTITATIVE ESTIMATION OF AVERAGE MEAN SURFACE CURVATURE (after R. T. DeHoff [41])

Consider an element,  $d\lambda$ , of a line intersection on an interface separating the phase of interest from all others in the system. The curvature,  $k$ , of this two-dimensional element of arc is defined by the relation

$$k = \frac{d\theta}{d\lambda} \quad (27)$$

where  $d\theta$  is the angle subtended by the element and is the angle between the normals placed at the ends of the line element. The average curvature of several individual elements or of an element of finite size is given by

$$\bar{k} = \frac{\oint k(\lambda) d\lambda}{\oint d\lambda} \quad (28)$$

Substituting (27) into (28) gives

$$\bar{k} = \frac{\int d\theta}{\lambda} \quad (29)$$

Since  $\bar{k}$  can contain both convex and concave elements of arc, the numerator of equation (29) must integrate to the net subtended angle; i.e., the algebraic sum of the angles subtended by each type of curved element.  $\lambda$  is the total length of elements of arc included in the average and is readily obtained through standard quantitative

metallographic procedures. Per unit area of test section through the structure  $\lambda$  is equivalent to  $L_A$  and from quantitative metallography

$$L_A = \frac{\pi}{2} N_L \quad (30)$$

where  $N_L$  is the number of intersections with the interface occurring per unit length of test line.

The net subtended angle may be obtained by two methods. On a two-dimensional section a closed loop of line intersection subtends a net angle of  $\pm 2\pi$  radians. If the loop encloses the solid phase it is defined as convex, and its net subtended angle is  $+ 2\pi$  radians. If the loop encloses the void space of the structure its net subtended angle is  $- 2\pi$  radians. Thus the net subtended angle of the total void-solid interface per unit area of the structure is given by

$$\theta_{A_{\text{net}}} = 2\pi (N_{A+} - N_{A-}) = 2\pi N_{A_{\text{net}}} \quad (31)$$

where  $N_{A_{\text{net}}}$  is the algebraic sum of the number per unit area of closed loops around the solid (positive) and around the void phase (negative). Substituting (31) into (29) gives the average curvature of the two-dimensional structure

$$\bar{\kappa} = 4 \frac{N_{A_{\text{net}}}}{N_L} \quad (32)$$

The net subtended angle may also be determined by counting the number of tangents which occur by sweeping the element of arc with test lines uniformly distributed in orientation. Since test lines sweeping over the element from opposite directions produce no new

tangents, only a semicircle of orientation range is required. The fraction of the uniformly distributed test lines which form a tangent with element  $d\lambda$  is the fraction of the circumference of the semicircle of orientation which lies within the subtended angle,  $d\theta$ , of the element of arc; i.e.,  $\frac{rd\theta}{\pi r} = \frac{d\theta}{\pi}$ . For  $N$  test lines, each sweeping over an area  $L^2$  of the specimen, the number of tangents formed with the sum of all elements per unit area of specimen sampled is

$$T_{A_{\text{tot}}} = \oint N \frac{d\theta}{\pi} \left( \frac{1}{NL^2} \right) = \oint \frac{d\theta}{\pi L^2} = \frac{\theta_{A_{\text{tot}}}}{\pi} \quad (33)$$

where  $\theta_{A_{\text{tot}}}$  is the total angle subtended by the total perimeter of void-solid interface per unit area sampled. As in the case of closed loops, convex and concave elements of boundary are defined with respect to the solid phase and the net subtended angle per unit area is given by

$$\theta_{A_{\text{net}}} = \pi (T_{A_+} - T_{A_-}) \quad (34)$$

where  $T_{A_+}$  is the number of tangents with convex elements per unit area and  $T_{A_-}$  is the number with concave elements. Substituting (34) into (29) gives

$$\bar{k} = 2 \frac{T_{A_{\text{net}}}}{N_L} \quad (35)$$

Equations (32) and (35) allow the determination of the curvature of line elements only. The mean curvature of an element of

surface is defined\* by

$$H = \frac{1}{r_1} + \frac{1}{r_2} = \kappa_1 + \kappa_2 \quad (36)$$

where  $\kappa_1$  and  $\kappa_2$  are the two principal normal curvatures. Over the entire surface of the system, the average value,  $\bar{H}$ , is defined by

$$\bar{H} = \frac{\iint H dS}{\iint dS} \quad (37)$$

Consider, as presented in Figure 42, the intersection of a plane with an element of surface. The curvature of this line of intersection is given by

$$\bar{\kappa}(\theta, \varphi, u, v) = \frac{1}{\sin \varphi} [\kappa_1(u, v) \cos^2 \theta + \kappa_2(u, v) \sin^2 \theta] \quad (38)$$

where  $\varphi$  and  $\theta$  specify relative orientation of the sectioning plane and the surface element.

To determine the average length of intersection of test planes with the element of surface for which equation (38) gives the curvature, both the orientation and position of the test planes with respect to the surface element and also the arc length for an average section must be considered. For sections uniformly distributed in orientation the fraction of sections that are contained within the orientation range available on each element of surface

---

\* This definition of mean curvature is used here for its direct correlation with the equations of capillarity (e.g., equation (5)). The arithmetic mean curvature as applied by DeHoff [41] in his original derivation is defined as  $\frac{1}{2}(\kappa_1 + \kappa_2)$ .

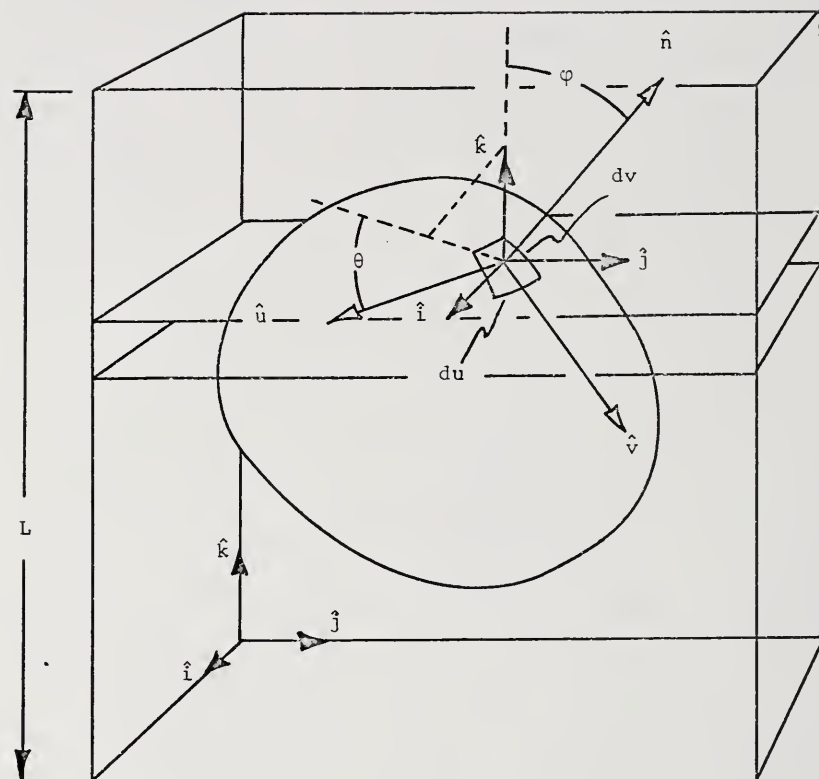


Figure 42. Orientation relationships that exist between an arbitrary element of surface ( $du dv$ ) and a sectioning plane;  $\hat{n}$  is the surface normal;  $\hat{u}$  and  $\hat{v}$  are the directions of principal curvature;  $\hat{k}$  is normal to the sectioning plane.

(i.e.,  $d\theta$ ,  $d\varphi$ ) is equal to the fraction of the area of a unit sphere in the same orientation range

$$f(\theta, \varphi) d\theta d\varphi = \frac{\sin \varphi d\theta d\varphi}{4\pi} \quad (39)$$

Substituting (39) and (38) into an equation of the form of (29) gives

$$\bar{k} = \frac{\int_0^\pi \int_0^{2\pi} \int_u \int_v [\kappa_1(u, v) \cos^2 \theta + \kappa_2(u, v) \sin^2 \theta] \frac{1}{\sin \varphi} \frac{\sin^2 \varphi}{4\pi} du dv d\theta d\varphi}{\int_0^\pi \int_0^{2\pi} \int_u \int_v \frac{\sin^2 \varphi}{4\pi} du dv d\theta d\varphi} \quad (40)$$

Integration yields

$$\bar{k} = \frac{2}{\pi} \frac{\int_u \int_v [\kappa_1(u, v) + \kappa_2(u, v)] du dv}{\int_s \int_s H dS} = \frac{2}{\pi} \frac{\int_s H dS}{\int_s dS}$$

or

$$\bar{k} = \frac{2}{\pi} \bar{H} \quad (41)$$

Equation (41) relates the average mean surface curvature to the average value of line curvature observed on two-dimensional sections through the structure. Substitution of (41) into (32) gives

$$\bar{H} = 2\pi \frac{N_{A_{\text{net}}}}{N_L} \quad (42)$$

and into (35) gives

$$\bar{H} = \pi \frac{T_{A_{\text{net}}}}{N_L} \quad (43)$$

All of the experimental determinations of  $\bar{H}$  of the void-solid interface in this research were accomplished through the application of equation (43).

# REFERENCES

- [1] F. N. Rhines, Reutte Plansee Proc. 3rd Seminar, Reutte/Tyrol, 1958, 38.
- [2] F. Saurwald, Koll. Z., 1943, 104, 144.
- [3] M. Yu. Balshin, Vestnik Metallopromish., 1936, 16 (17), 87.
- [4] M. Yu. Balshin, Ibid., 1936, 16 (19), 82.
- [5] M. Yu. Balshin, Ibid., 1936, 16 (18), 91.
- [6] W. D. Jones, "The Principles of Powder Metallurgy," p. 158. 1937: London (E. Arnold, Ltd.).
- [7] C. C. Balke, Iron Age, 1941, 147 (16), 23.
- [8] P. E. Wretblad and J. Wulff, "Powder Metallurgy," Chap. 4. 1942: Cleveland (American Society for Metals).
- [9] F. N. Rhines, Trans. AIME, 1946, 166, 474.
- [10] J. Frenkel, U.S.S.R. J. Phys., 1945, 9, 385.
- [11] C. Herring, J. App. Phys., 1950, 21 (5), 437.
- [12] H. Udin, A. J. Shaler and J. Wulff, Trans. AIME, 1949, 185, 186.
- [13] B. Ya. Pines, J. Tech. Phys., 1946, 16, 737.
- [14] A. J. Shaler and J. Wulff, Ind. and Eng. Chem., 1948, 40, 838.
- [15] A. J. Shaler, Trans. AIME, 1949, 185, 796.
- [16] R. F. Walker, J. Amer. Cer. Soc., 1955, 38 (6), 187.
- [17] F. V. Lenel, J. G. Early and G. S. Ansell, Trans. AIME, 1964, 230, 1641.
- [18] F. N. Rhines, Powder Met. Bull., 1948, 3 (2), 28.
- [19] G. C. Kuczynski, J. Metals, 1949, 1 (2), 169.
- [20] G. C. Kuczynski, J. App. Phys., 1949, 20, 1160.

- [21] J. H. Mackenzie and R. Shuttleworth, Proc. Phys. Soc. [B], 1949, 62 (12), 833.
- [22] F. N. Rhines, C. E. Birchenall and L. A. Hughes, Trans. AIME, 1950, 188, 328.
- [23] G. A. Geach and F. O. Jones, Research, 1949, 2, 493.
- [24] B. H. Alexander and R. W. Balluffi, J. Metals, 1950, 188, 1219.
- [25] L. C. Correa da Silva and R. F. Mehl, J. Metals, 1951, 191, 155.
- [26] A. L. Pranatis, L. S. Castleman and L. Seigle, First, Second and Third Prog. Rep., Sylvania Res. Lab., AEC Contract AT(30-1) GEN 366, Proj. No. 1862, 1957.
- [27] G. C. Kuczynski, Acta Met., 1956, 4, 58.
- [28] B. H. Alexander and R. W. Balluffi, Prog. Rep. AEC Contract AT(30-1) GEN 367, 1950.
- [29] C. Herring, J. App. Phys., 1950, 21, 301.
- [30] R. T. DeHoff, D. H. Baldwin and F. N. Rhines, Reutte Plansee Proc. 4th Seminar, Reutte/Tyrol, 1962, 171.
- [31] T. L. Wilson and P. G. Shewmon, Trans. AIME, 1966, 236, 48.
- [32] P. W. Clark and J. White, Trans. Brit. Cer. Soc., 1950, 49 (7), 305.
- [33] P. W. Clark, J. H. Cannon and J. White, Ibid., 1953, 52 (1), 1.
- [34] F. N. Rhines and H. S. Cannon, Trans. AIME, 1951, 191, 529.
- [35] J. Williams and K. H. Westnacott, AERE Report M/R No. 1143, 1953.
- [36] M. J. Salkind, F. V. Lenel and G. S. Ansell, Trans. AIME, 1965, 233, 39.
- [37] G. Arthur, J. Inst. Metals, 1954, 83, 329.
- [38] R. T. DeHoff, R. A. Rummel, H. P. LaBuff and F. N. Rhines, "Modern Developments in Powder Metallurgy," p. 310. 1966: New York (Plenum Press).
- [39] L. K. Barrett and C. S. Yust, "Progressive Shape Changes in the Void During Sintering," Submitted for Publication.



- [40] F. N. Rhines, "The Sorby Centennial Symposium on the History of Metallurgy," Ed. by C. S. Smith, Chap. 26. 1965: New York (Gordon and Breach).
- [41] R. T. DeHoff, Trans. TMS-AIME, 1967, 239, 617.
- [42] J. Cahn, Ibid., 1967, 239, 610.
- [43] E. Aigeltinger, University of Florida, Private Communication.
- [44] F. N. Rhines, Final Report, AEC Contract AT(30-1)-1826, 1959.
- [45] F. V. Lenel, H. H. Hausner, E. Hayashi and G. S. Ansell, Powder Met., 1961, 12 (8), 25.
- [46] F. Young, Masters Thesis, University of Florida, 1963.
- [47] P. Schwarzkopf, "Powder Metallurgy," p. 88. 1947: New York (Macmillan Co.).
- [48] W. D. Jones, "Fundamental Principles of Powder Metallurgy," p. 350. 1960: London (Edward Arnold, Ltd.).
- [49] J. Willard Gibbs, "The Scientific Papers of J. Willard Gibbs," p. 219. 1961: New York (Dover).
- [50] R. Shuttleworth, Proc. Phys. Soc. [A], 1950, 63 (5), 444.
- [51] M. Faraday, Phil. Trans., 1857, 147, 145.
- [52] J. C. Chapman and H. L. Porter, Proc. Roy. Soc. [A], 1911, 83, 65.
- [53] H. Schottky, Gött. Nahr. Math. Physik. Klasse, 1912, 71, 480.
- [54] I. Sawai and M. Nishida, Z. Anorg. Chemie, 1930, 190, 375.
- [55] G. Tammann and W. Boehme, Ann. Phys., 1932, 12, 820.
- [56] J. C. Fisher and C. G. Dunn, AEC Publ. RL463, 1950.
- [57] H. Udin, Trans. AIME, 1951, 191, 63.
- [58] T. Slean, University of Florida, Private Communication.
- [59] M. Inman and H. Tipler, Met. Reviews, 1963, 8 (30), 105.
- [60] F. N. Rhines and R. T. DeHoff, "The Geometry and Mechanism of Sintering," Submitted for Publication.
- [61] R. L. Fullman, Trans. AIME, 1953, 197, 447.

- [62] R. T. DeHoff and T. Slean, University of Florida, Private Communication.
- [63] C. A. Calow and C. R. Tottle, Powder Met., 1965, 8 (15), 1.
- [64] W. Dawihl and W. Rix, Z. Metall., 1949, 40, 115.
- [65] B. H. Alexander, M. Dawson and H. P. Kling, J. App. Phys., 1951, 22, 439.
- [66] G. D. McAdam, J. Iron Steel Inst., 1951, 168, 346.
- [67] J. Gillard, Masters Thesis, University of Florida, 1964.
- [68] A. L. Pranatis and G. M. Pound, J. Metals, 1955, 7, 664.
- [69] C. Barrett and O. D. Sherby, Trans. TMS-AIME, 1964 230, 1322.
- [70] J. Lemons, University of Florida, Private Communication.
- [71] E. Eilbeck, University of Florida, Private Communication.
- [72] B. H. Alexander, G. Kuczynski and M. Dawson, J. App. Phys., 1951, 22, 439.
- [73] E. R. Hayward and A. P. Greenough, J. Inst. Metals, 1959, 88, 217.
- [74] A. T. Price, H. Holl and A. P. Greenough, Acta Met., 1964, 12, 49.
- [75] R. Courant and H. Robbins, "What is Mathematics," 7th Ed., Chap. 5. 1956: London (Oxford Univ. Press).
- [76] W. Pfann and D. Hagelbarger, J. App. Phys., 1956, 27, 12.

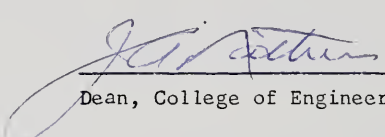
## BIOGRAPHICAL SKETCH

Roger Allen Gregg was born July 19, 1938, at Lenoir, North Carolina, the eleventh child of Mr. and Mrs. William L. Gregg, Sr. In June, 1956, he was graduated from Lenoir High School. He attended North Carolina State University from which he received the degrees of Bachelor of Science with Honors (June, 1960) and Master of Science (January, 1962) in Metallurgical Engineering. From 1962 to 1963 he was employed by Pratt and Whitney Aircraft Company in North Haven, Connecticut. From September, 1963, until the present time he has pursued the degree of Doctor of Philosophy at the University of Florida.

The author is married to the former Susan Elizabeth Davis and is the father of three children. He is a member of Sigma Xi, Alpha Sigma Mu, Tau Beta Pi, American Society for Metals and The Metallurgy Society of the American Institute for Metallurgical, Mining and Petroleum Engineers.


This dissertation was prepared under the direction of the chairman of the candidate's supervisory committee and has been approved by all members of that committee. It was submitted to the Dean of the College of Engineering and to the Graduate Council, and was approved as partial fulfillment of the requirements for the degree of Doctor of Philosophy.

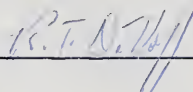
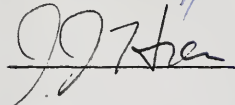
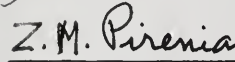
June, 1968

  
\_\_\_\_\_  
Dean, College of Engineering

\_\_\_\_\_  
Dean, Graduate School

Supervisory Committee:

  
\_\_\_\_\_  
Chairman

  
\_\_\_\_\_  
 (for R. E. Reed-Hill)  
 (for R. G. Blake)  
\_\_\_\_\_  
\_\_\_\_\_